Article:
Jaervinen, A. E., Giroud, C., Groth, M. et al. (2016) Comparison of H-mode plasmas in JET-ILW and JET-C with and without nitrogen seeding. Nuclear Fusion. 046012. ISSN: 1741-4326

https://doi.org/10.1088/0029-5515/56/4/046012

Comparison of H-mode Plasmas in JET-ILW and JET-C with and without Nitrogen Seeding

A. E. Jaervinen[1], C. Giroud[2], M. Groth[1], P.Belo[2], S. Brezinsek[3], M. Beurskens[2], G. Corrigan[2], S. Devaux[4], P. Drewelow[5], D. Harting[2], A. Huber[3], S. Jachmich[6], K. Lawson[2], B. Lipschultz[7], G. Maddison[2], C. Maggi[2], C. Marchetto[8], S. Marsen[4], G. F. Matthews[2], A.G. Meigs[2], D. Moulton[2], B. Sieglin[5], M. F. Stamp[2], S. Wiesen[3], and JET Contributors∗

EUROfusion Consortium, JET, Culham Science Centre, Abingdon, OX14 3DB, UK

[1]Aalto University, Association Tekes, FI-00076 AALTO, Espoo, Finland
[2]Culham Centre for Fusion Energy, Association CCFE, Abingdon, UK
[3]Forschungszentrum Jülich GmbH, Institut für Energie- und Klimaforschung – Plasmaphysik, 52425 Jülich, Germany
[4]Max-Planck Institute for Plasma Physics, Greifswald, Germany
[5]Max-Planck Institute for Plasma Physics, Garching, Germany
[6]Association "Belgium State", Lab. for Plasma Physics, Brussels, Belgium
[7]University of York, YO10 5DD York, UK
[8]Association ENEA IFP-CNR, Milan, Italy

E-mail contact of main author: aaro.jarvinen@aalto.fi

Abstract.

In high confinement mode, highly shaped plasmas with edge localized modes in JET, and for heating power of 15 – 17 MW, the edge fluid code EDGE2D-EIRENE predicts transition to detachment assisted by nitrogen at the low field side (LFS) target when more than 50% of the power crossing the separatrix between ELMs is radiated in the divertor chamber, i.e. ~ 4 MW. This is observed both in the ITER-like wall (JET-ILW) and in the carbon wall (JET-C) configurations and is consistent with experimental observations within their uncertainty. In these conditions, peak heat fluxes below 1 MW/m2 are measured at the LFS target and predicted for both wall configurations. When the JET-C configuration is replaced with the JET-ILW, a factor of two reduction in the divertor radiated power and 25 – 50% increase in the peak and total power deposited to the LFS divertor plate is predicted by EDGE2D-EIRENE for unseeded plasmas similar to experimental observations. At the detachment threshold, EDGE2D-EIRENE shows that nitrogen radiates more than 80% of the total divertor radiation in JET-ILW with beryllium contributing less than a few %. With JET-C, nitrogen radiates more than 70% with carbon providing less than 20% of the total radiation. Therefore, the lower intrinsic divertor radiation with JET-ILW is compensated by stronger nitrogen radiation contribution in simulations leading to detachment at similar total divertor radiation fractions. 20 – 100% higher deuterium molecular fraction in the divertor recycling fluxes is predicted with light JET-C materials when compared to heavy tungsten. EDGE2D-EIRENE simulations indicate that the stronger molecular contribution can reduce the divertor peak power deposition in high recycling conditions by 10 – 20% due to enhanced power dissipation by molecular interaction.
Number of words in the abstract: 276

1. Introduction

Full metal plasma facing components (PFCs) are foreseen in the next step fusion devices to optimize the reactor duty cycle by minimizing component erosion and tritium retention [1]. To address the impact of full metal PFCs on the operational boundaries of next step devices, JET was converted from an all carbon (JET-C) to the ITER-like wall (JET-ILW) with bulk beryllium limiters and tungsten divertor [2]. As a result, a factor of 10 reduction in the carbon radiation levels and fuel retention rates were experimentally confirmed [3, 4]. Unexpectedly, the energy confinement time was reduced by 30 – 40% in highly shaped baseline high confinement mode (H-mode) plasmas with edge-localized modes (ELMs) [5 – 8]. This reduction was mainly associated with degraded pedestal performance, whereas pressure peaking between the pedestal and the central plasma remained unchanged within 5% [5]. The lost confinement was largely recovered with nitrogen seeding, indicating a role of low charge state impurities in the formation and performance of the H-mode pedestal in JET [5 – 8]. It was also experimentally observed that a high-triangularity configuration was essential to reach a significant 40% confinement recovery with nitrogen seeding, whereas in low-triangularity the confinement was improved by about 15% only [8].

With the change from JET-C to JET-ILW, a significant reduction of scrape-off layer (SOL) radiation due to intrinsic impurities was expected. This is due to strong radiative potential of carbon in the divertor relevant electron temperatures of 10 – 30 eV, whereas beryllium radiation peaks at a few eV only with a peak radiative potential about a factor of 3 lower than that of carbon. Tungsten, on the other hand, is expected to radiate dominantly inside the pedestal. This conceptual radiation physics difference between the JET-C and JET-ILW configurations is indeed supported by EDGE2D-EIRENE simulations presented in this study, as well as documented for low-confinement mode (L-mode) plasmas in [9 – 12]. As a result of the reduced carbon concentrations, 30% reduction of the total radiative power, and a factor 2 reduction in the divertor radiation was reported for the baseline ELMy H-mode plasmas in JET [5]. Consistently, a 30% reduction of SOL radiation was reported for L-mode plasma in JET [9].

Since the radiative potential of nitrogen is similar to that of carbon, nitrogen seeding is expected to provide radiation distributions close to those observed in the carbon wall plasmas. In fact, with nitrogen seeding these H-mode plasmas with JET-ILW were able to recover the divertor radiation levels observed in the nitrogen seeded plasmas in JET-C [5, 13]. Low field

side (LFS) divertor detachment between ELMs was obtained with nitrogen injection in both JET-C and JET-ILW with only a modest impact on the plasma performance [5, 6, 14, 15]. These findings are also inline with EDGE2D-EIRENE simulations presented in this study.

Furthermore, the change from JET-C to JET-ILW is expected to impact plasma ion recycling properties at the PFCs. Since the surface reflection coefficient for impinging particles is expected to increase with increasing substrate to projectile mass ratio, tungsten PFCs are expected to increase the contribution of fast reflections versus thermal re-emission in the recycling process [16]. This results into a stronger deuterium atom versus molecular component in the recycling fluxes with tungsten compared to carbon PFC [17, 18]. The stronger reflectivity of tungsten PFCs leads also to higher energy reflectivity, thereby heating the SOL plasmas in JET-ILW relative to JET-C for otherwise similar boundary conditions [19]. The EDGE2D-EIRENE simulations presented in this study indicate that due to these effects the LFS strike point electron temperatures is increased by up to a factor 2 for a given upstream density, increasing the LFS detachment threshold electron collisionality and density at the LFS mid-plane by 5 – 10%.

This study concentrates on an overlapping series of deuterium fuelled and nitrogen seeded baseline ELMy H-mode plasmas obtained in JET-C and JET-ILW configurations with 15 – 17 MW of input power at plasma current of 2.5 MA and at toroidal magnetic field at the magnetic axis of 2.7 T [5 – 8]. The plasmas were conducted in a high-triangularity configuration, $\delta \sim 0.4$, with the low field side (LFS) strike point on the horizontal target and the high field side (HFS) strike point on vertical target with an edge safety factor about 3.5 (Fig.1). Deuterium was injected at the HFS target, and nitrogen was seeded at the LFS target into the common SOL. The deuterium fuelling levels in the unseeded JET-C plasmas were in the range of 0.22 – 6e22 e/s, while in JET-ILW a range of 0.9 – 3.5e22 e/s was obtained. In terms of nitrogen seeding the investigated plasmas are divided into 4 categories: 1) Unseeded ($\Gamma_{N2} \sim 0$ e/s), 2) Low-N_2 ($\Gamma_{N2} \sim 1 – 1.5$e22 e/s), 3) Medium-N_2 ($\Gamma_{N2} \sim 2 – 2.5$e22 e/s), and 4) High-N_2 ($\Gamma_{N2} \sim 3.5 – 4.5$e22 e/s). Most of the experimental observations have been documented in previous publications [5 – 8, 13 – 15, 27 – 29]. In this study, the SOL characteristics of these plasmas are further analyzed and compared against EDGE2D-EIRENE simulations.

2. EDGE2D-EIRENE setup

EDGE2D-EIRENE was executed for steady-state, inter-ELM simulations for these discharges to validate the model for predictions of radiation distributions and divertor conditions. Furthermore, the simulations are used to assess the hierarchy of the physics processes in the experimentally observed divertor radiation and detachment characteristics and neutral recirculation patterns in the D_2-fuelled and N_2-seeded plasmas in JET-C and JET-ILW. The main boundary conditions in the simulations presented in this study are similar to those used in [15]. In the divertor chamber below the X-point, spatially constant cross-field transport parameters are used as specified in [15]. Identical particle diffusivities are used for all particle species. The simulations do not capture the experimentally observed increase of pedestal temperatures with nitrogen seeding in JET-ILW or the pedestal temperatures in JET-C. This is caused by the fact that the edge transport barrier heat conductivity profiles are adjusted to reproduce the experimentally measured pedestal electron temperature profiles in the unseeded JET-ILW simulations with lower pedestal temperatures.. Nevertheless, sensitivity scans show that the JET-C like pedestal temperatures can be reproduced in the simulations by scaling the edge transport barrier heat conductivities inside the separatrix down by a factor of 2 – 3 with a negligible impact on the SOL plasma solution. In other words, as long as the power crossing the separatrix and the LFS mid-plane electron density do not change, and the transport coefficient in the SOL are not changed, the SOL plasma solution remains practically the same.

Physical sputtering of beryllium and carbon as given by Eckstein et al. [30] are used in the simulations. Flux dependent carbon chemical sputtering yield of the Roth and Pacher 2003 with fixed 1e19 $m^{-2}s^{-1}$ main wall flux is used [31]. The chemical sputtering yield for carbon is multiplied by a factor of 2 to increase the carbon radiation levels in the simulations. Sensitivity scans with this multiplication factor increased all the way up to 30 to match the measured radiation levels will also be presented in this paper. ADAS 96 atomic rates are used for fuel and impurity species [32]. To obtain converged EDGE2D-EIRENE solutions in detached plasmas with the strike point electron temperatures about or below 0.5 eV, nitrogen radiation was forced to go to zero in electron temperatures below 0.3 eV. Without this step, the plasma temperatures would drop down to the lower limit value (0.05 eV) in the code, and due to numerical reasons, which are not fully resolved by the time of writing this report, the solver would cease to run at time-steps that are acceptable for reaching a converged solution within pragmatic time-scales.

Tungsten impurities are not included in the main simulations in this study. However, sensitivity simulations with tungsten in this study, based on the unseeded plasmas, indicate that more than 90% of tungsten radiation occurs inside the separatrix. Therefore, for the SOL, this equals to reduction of the power crossing the separatrix or input power into the computational domain. In other words, the dominant impact of tungsten on the SOL plasma solution is implicit through the core radiation and reduction of the power crossing the separatrix, and is included in the uncertainty of the input power in the simulations. Furthermore, this approach simplifies the simulation analysis process since (1) the dominant source of tungsten occurs presumably during ELMs, which are not included in these simulations [33, 34], (2) the main source of tungsten that eventually contaminates the confined plasmas may be located outside the divertor area where the plasma-surface interaction is not modeled in high detail in these simulations due to the plasma grid not extending to the main chamber wall, (3) prompt re-deposition is foreseen to be very large ~ 50 – 99% for tungsten but not included in EDGE2D-EIRENE as it stands [33 – 36], (4) the bundled fluid approach for modelling trace tungsten in the divertor plasma has not yet been fully verified against kinetic or quasi-kinetic simulations, and [33 – 36] (5) the tungsten transport in the main SOL and inside the pedestal is foreseen to be strongly impacted by neo-classical, turbulent and centrifugal transport effects, which are not taken properly into account in the EDGE2D-EIRENE simulations.

Nitrogen is assumed fully recycling in this study, whereas all the other impurities are assumed non-recycling. Full recycling is an extreme assumption for nitrogen since nitrogen is chemically active, forms ammonia and partially sticks to the wall material [37]. However, one might argue that the divertor surfaces reach near to equilibrium nitrogen concentration soon enough in the experimental nitrogen seeding scan, such that the effective nitrogen recycling coefficient on the divertor surface approaches full recycling. In the main chamber this assumption is presumably more questionable. Nitrogen molecules are not included in the model. Instead, nitrogen particles are injected as atoms. However, in previous investigations, the impact of nitrogen molecule break-up on the density distribution of singly ionized nitrogen particles was found to be less than 5% [15]. Nitrogen injection levels are feedback controlled in the simulations to scan through the radiated power levels observed experimentally.

For neutral deuterium atoms and molecules, and impurity atoms, the Kotov-2008 EIRENE model is used in most of the simulations in this study [38, 39]. At the divertor

targets, standard Bohm-Chodura sonic to supersonic plasma flow is assumed and the sheath-heat transmission coefficients for electrons and ions are set to 4.5 and 2.5, respectively [40 – 42]. In these studies, cross-field drifts and currents are omitted to avoid the extra numerical difficulties associated with EDGE2D-EIRENE simulations including these terms. Due to these reasons, dedicated cross-field drift studies with EDGE2D-EIRENE are often conducted with carefully optimized grids and without impurities, as is done in [43]. The omission of drifts in this study is likely to compromise the ability of the simulations to capture the experimentally observed HFS and LFS divertor conditions simultaneously. The greatest impact of cross-field drifts on the plasma solution in L-mode plasmas are observed in low- and high-recycling divertor conditions, whereas in detached conditions the radial temperature gradients in the divertor plasmas are reduced significantly compared to high recycling plasmas resulting into reduction of the electric potential gradients, therefore, reducing the **ExB**-drive and the impact of drifts on the plasma solution [44, 45].

An EDGE2D-EIRENE plasma solution is considered converged in this study if the simulation has reached an asymptotic state with the characteristic time-scales for the separatrix electron densities and temperatures at the LFS mid-plane, and the total particle, energy, and impurity contents in the computational domain longer than 1s. Therefore, within characteristic inter-ELM time in the investigated plasmas, 20 – 50ms, these parameters evolve less than 5%.

3. Experimental observations

a. Unseeded plasmas

Without injection of extrinsic impurities as plasma radiators, for a given deuterium fuelling rate the LFS divertor leg in the JET-ILW plasmas is in a low-radiation, low-recycling regime characterized by (1) a factor of 2 – 3 lower LFS divertor leg radiated power, (2) 20 – 50% higher LFS divertor target peak electron temperature, and (3) a factor of 2 lower LFS divertor target peak saturation current than measured in the JET-C configuration (Figs. 2 b, c, d). The data is organized as a function of deuterium fuelling rate instead of SOL separatrix density due to uncertainties of the latter. The uncertainty of the LFS mid-plane separatrix location, as given by the magnetic equilibrium reconstruction, is a few cm, which is comparable to the gradient length of the measured electron density in the vicinity of the separatrix. However, it can be observed that, within the large uncertainty provided by the diagnostics resolution, the two wall configurations reach the same $n_{e,LFS\text{-}mp}$ for a given

deuterium fuelling rate (Fig. 2a). The shift of the separatrix is obtained for both wall configurations by picking up the $n_{e,LFS\text{-}mp}$ values from EDGE2D-EIRENE predictions that provide the closest representation of the measured LFS divertor conditions in the plasmas with the lowest deuterium fuelling rates. The measured LFS mid-plane electron density profiles are shifted, such that the $n_{e,LFS\text{-}mp}$ values match with the predicted ones. These LFS mid-plane separatrix shifts are used for all the other plasmas with and without impurity seeding, assuming that the difference between the real and EFIT separatrices does not change between shots.

30% lower radiative power fraction, and a factor of 2 lower divertor radiation levels were experimentally measured in the unseeded plasmas in JET-ILW than in JET-C (Fig. 12 in [5]). Integration over the tomographic reconstructions of the bolometer system indicate that the most significant reduction occurs in the LFS divertor, whereas in the HFS divertor the reduction is about 20% only (Fig. 2b). These observations are consistent with the line-integral values of the divertor channels of the vertical bolometer system, providing confidence that these observations cannot be explained solely by spatial uncertainties of the reconstruction itself (Fig. 5a). Consistently, the electron temperature at the LFS plate is about 20 – 50% higher and the peak saturation current at the LFS plate is about a factor of 2 lower in JET-ILW than in JET-C for a given deuterium fuelling rate (Figs. 2c, d). These findings are consistent with carbon being a strong radiator in the LFS divertor leg volume electron temperatures in the range of 10 – 30 eV, whereas strong beryllium or deuterium radiation is not expected at these temperatures. The onset of detached conditions at the LFS plate, indicated by reduction of the peak saturation current, was observed without nitrogen seeding in the JET-C at the deuterium fuelling levels exceeding 2.8e22 e/s [14] (Fig. 2d). However, the integral particle fluxes to the LFS plate were not reduced significantly [14]. The unseeded plasmas in JET-ILW remained attached throughout the fuelling scan (Fig. 2d).

At the HFS divertor, peak electron temperatures at or less than 10 eV and peak saturation currents below 0.5 – 1 MA/m^2 are measured by the divertor Langmuir Probes in both configurations throughout the deuterium injection scans indicating detached or partially detached conditions. In these conditions, deuterium and beryllium radiation can become significant compared to carbon radiation due to low electron temperatures in the range of a few eV and high electron densities in the range of a few 10^{20} m^{-3} in the HFS divertor volume. Consistently, comparable HFS divertor leg radiation levels are experimentally observed in the unseeded JET-ILW and JET-C plasmas (Figs. 2a, 4a, e, 5a). However, the HFS divertor

Langmuir Probe analysis is compromised by the fact that the HFS strike point is located at the gap between the JET divertor tiles 1 and 3, resulting into a distinctive gap around the strike point in the obtained electron temperature and saturation current profiles. Therefore, the actual peak values of the HFS divertor electron temperature and saturation current profiles may not be captured by the divertor Langmuir Probes, and the measured values represent lower boundary, shown here for completeness.

In the JET-C, the peak power load at the LFS plate was reduced from about 6 – 16 MW/m^2 at the lowest deuterium fuelling level (0.3e22 e/s) down to 3 – 4 MW/m^2 at the medium fuelling levels (1.5 – 4.5e22 e/s) and finally down to around 2 – 3 MW/m^2 at the maximum investigated deuterium fuelling level (6.0e22 e/s) without nitrogen seeding as measured by the IRTV system [14]. In JET-ILW, the coverage of IRTV data for this series of discharges was not as comprehensive as it was in the JET-C series. However, values in the range of 5 MW/m^2 were measured for the medium deuterium fuelling levels (3.2e22 e/s) [6], indicating 20 – 30% higher LFS plate power deposition for a given fuelling rate in JET-ILW compared to JET-C, consistent with previous L-mode studies [9].

b. Nitrogen seeded plasmas

With injection of nitrogen in JET-ILW, the divertor radiation power measured in the nitrogen seeded JET-C plasmas are recovered both in the LFS and HFS divertor legs (Fig. 3 b). Similar to the unseeded plasmas, the nitrogen seeded plasmas in JET-C and JET-ILW obtain similar $n_{e,LFS\text{-}mp}$-values within the uncertainty for similar divertor radiation values (Fig. 3a). Whereas without impurity seeding the JET-ILW divertor radiation distribution is dominated by the HFS divertor leg, with a low to medium nitrogen injection both the radiation distribution and the line-integrated values of the vertical divertor bolometer channels become very similar to those observed in the JET-C environment in the unseeded or low N_2-injection plasmas (Figs. 4 a – c, e – f; Figs. 5 a – c). With further N_2-injection in both JET-C and JET-ILW, it is observed that the radiation front in the LFS divertor leg shifts towards and concentrates at the low-field side of the X-point. However, the spatial accuracy of the bolometric system does not allow discrimination whether this radiation front is inside or outside the confined region. These observations indicate that nitrogen indeed provides radiative characteristics close to those of carbon, therefore, recovering the typical JET-C like divertor radiation levels and distributions in JET-ILW. The highly localized radiation front at the low-field side X-point appears to be correlated with the onset of LFS divertor detachment

in both configurations (Fig. 3 d). As documented in [15], this is presumably related to reduction of the divertor leg electron temperatures below 5 eV, for which nitrogen does not radiate strongly anymore, whereas the temperatures upstream from the X-point are not reduced below 40 eV due to shallow magnetic pitch angle at the X-point and cross-field heat source from the confined plasma. Therefore, the volume of the suitable electron temperatures for nitrogen radiation, 10 – 30 eV, concentrates poloidally to the X-point. In fact, since divertor detachment is likely to require a significant divertor volume with electron temperatures below 5 eV to allow enough volumetric momentum dissipation between the deuterium ionization front and the divertor target, detached scenarios with significant impurity radiation are likely to be generally characterized by an impurity radiation front at or above the X-point, where the electron temperatures are high enough for impurity radiation.

LFS detachment between ELMs induced by nitrogen is measured to occur in both JET-C and JET-ILW when about 40 – 50% of the estimated power crossing the separatrix is radiated in the divertor, corresponding to an absolute divertor radiated power level about 4 MW (Fig. 3 d). In these divertor conditions, Stark broadening electron density profiles in the LFS divertor leg in JET-ILW show a shift of the peak electron density front upstream from the target (Fig. 6). In this profile, the measured densities in the LFS divertor leg are in the range of 4e20 m^{-3} reducing down to about 1e20 m^{-3} in front of the strike-point. As will shown in the section 4-c in this paper, this shift of the peak electron density front away from the target in an impurity radiation induced detachment is a physics feature that the EDGE2D-EIRENE simulations struggle to reproduce in numerically well behaving plasma solutions.

With low to medium nitrogen injection in JET-ILW, the divertor radiation levels and divertor particle fluxes increase relative to the unseeded base case, thereby recovering the higher LFS radiation, higher recycling regime observed in the unseeded JET-C plasmas (Figs. 3 b, d). Interestingly, when this occurs the energy confinement levels are also recovered close to the values observed in the JET-C discharges [5, 6]. The peak confinement in JET-ILW is obtained at the boundary of high-recycling and detached LFS divertor conditions, whereas in JET-C the confinement is observed to reduce monotonically with increasing nitrogen seeding [5, 6]. In detached conditions with nitrogen seeding, both configurations reach LFS divertor power fluxes at or below 1 MW/m^2, which is around the detection limit of the IRTV system.

The increase of the energy confinement in JET-ILW is associated with a 20 – 30 % increase in the pedestal electron density and with a 30 – 40% increase in the pedestal electron

temperature, thereby also approaching the pedestal densities and temperatures observed in the corresponding JET-C plasmas [5, 6]. The EDGE2D-EIRENE simulations presented in the next section indicate that the neutral deuterium flux crossing the separatrix around the X-point increases with increasing divertor radiation, imposed either with carbon or nitrogen. Therefore, increasing divertor transparency to recycling neutrals with increasing divertor radiation can well be a contributor in the observed increase of pedestal density.

4. EDGE2D-EIRENE interpretations

a. Impact of deuterium reflection on JET-C and JET-ILW PFCs on the divertor plasma properties

It is experimentally very challenging to isolate the impact of wall recycling properties on the SOL conditions from the impact of other changes in the SOL radiation characteristics, following the change from JET-C to JET-ILW. Therefore, EDGE2D-EIRENE simulations are applied to isolate and characterize the impact of the recycling changes on the SOL conditions. In this section, a series of pure deuterium EDGE2D-EIRENE simulations without any impurity contamination were simulated with the two wall configurations to characterize the impact of the deuterium reflectivity of carbon and tungsten PFCs on the SOL conditions.

i) Impact of JET-ILW and JET-C PFCs on the D_2 density in the divertor plasmas

Consistent with previous publications [17, 18, 46, 47], the EDGE2D-EIRENE simulations predict 20 – 100% higher molecular fraction in the divertor recycling fluxes for JET-C when compared to JET-ILW (Fig. 7a). The molecular fraction is predicted to reduce as a function of the divertor electron temperature. The simulations show a log-linear relation between the molecular fraction and the strike point electron temperature at the LFS divertor plate. These log-linear fits for the JET-C and JET-ILW simulations can be written as:

$$f_{D_2,\text{JET-C}} \approx [-7 * \ln(T_{e,\text{peak, LFS}}) + 82]\% \quad (1)$$

$$f_{D_2,\text{JET-ILW}} \approx [-9 * \ln(T_{e,\text{peak, LFS}}) + 58]\% \quad (2).$$

According to these log-linear fits, in detached conditions with LFS target electron temperatures below 2 eV, a molecular fraction about 55 – 80% is predicted for JET-ILW, whereas a fraction about 80 – 100% is predicted for JET-C. In high-recycling conditions these fractions become 40 – 55% for JET-ILW and 65 – 70% for JET-C, finally reducing down to

about 20 – 30% in JET-ILW and to about 55% in JET-C in conditions with LFS divertor temperatures above 20 – 30 eV. Consistent with higher deuterium reflectivity and atomic fraction in the divertor recycling fluxes, the energy reflection fraction in the divertor recycling fluxes in JET-ILW is predicted to be about 60 +/- 5%, and in JET-C about 30 +/- 5% (Fig. 7b). The total energy reflection fraction shows only a weak dependence on the divertor plasma regime in the simulations. As a result of the higher molecular fraction in the divertor recycling fluxes, the molecular density relative to the total neutral deuterium density in the divertor chamber is predicted to be 20 – 100% higher in JET-C than in JET-ILW (Fig. 7c). However, since ELMs are omitted in these steady-state simulations, the impact of ELM heat pulses on the PFCs outgassing and recycling properties, as well as on the time evolution of the divertor conditions, is not captures by the simulations presented here [48]. These are also expected to impact the deuterium molecular fraction in the divertor plasmas.

ii) Impact of the reduced D_2 density in JET-ILW on the LFS detachment characteristics and SOL conditions

Since the elastic collision between deuterium molecules and ions is typically observed to be one of the dominant momentum loss mechanism in tokamak divertor detachment modelling [38, 39, 49 – 51], it is expected that the reduced molecular fraction in the divertor plasma would adversely impact the formation of the neutral friction zone in JET-ILW relative to JET-C. However, unexpectedly, the total pressure ratio between the LFS divertor target and the LFS mid-plane does not change for a given strike point electron temperature (Fig. 7 d). Therefore, the simulations indicate that, as long as the peak electron temperature at the LFS plate is given, the pressure reduction between the LFS mid-plane and the LFS divertor plate does not change, even though the molecular density in the divertor plasma does. The impact of the wall material on the divertor pressure loss in the simulations is, hence, implicit via reduction of the peak target electron temperature for a given set of machine control parameters, such as plasma density, input power, or impurity seeding rate. In fact, detailed comparison of the momentum loss terms in the LFS divertor leg between the JET-C and JET-ILW simulations show that the sum of the atomic and molecular momentum losses remains the same between the configurations within 10%.

It is also observed in the simulations that even in the attached conditions the pressure-ratio between the LFS target and the LFS mid-plane is not exactly one but in the range of 0.7 – 0.8 due to residual recycling momentum losses and cross-field spreading of momentum in

the divertor plasma by viscosity effects and particle diffusion. The impact of cross-field spreading of momentum was investigated for the lowest density (collisionality), pure deuterium, ILW simulations, by setting the cross-field diffusivity below the X-point down to 0.001 m^2/s and scaling down the cross-field diffusivity by a factor of 100 and letting the plasma solution evolve for 100 ms. After this period, the solution obtains total hydrodynamic pressure balance between the LFS strike point and the LFS mid-plane within 4.5%.

In both wall configurations, the LFS plate peak pressures are predicted to reduce relative to the mid-plane separatrix pressures when the LFS plate electron temperatures are reduced below 4 – 6 eV (Fig. 7d). The plate pressures reach the level of 10% of the mid-plane pressures at the plate electron temperatures about 0.5 eV. Reducing the plate electron temperatures further down to 0.2 eV, the LFS plate pressure can be reduced down to the level of a few % of the mid-plane pressure. The peak saturation current in the simulations rolls over at about $T_e \sim 4 – 6$ eV, when the peak divertor pressure is predicted reduce relative to the upstream pressure (Fig. 7e). In these conditions, the peak heat flux at the LFS divertor plate is reduced to levels less than 1 MW/m^2 (Fig. 7f). The peak electron density, on the other hand, continues to increase with reducing divertor temperature until $T_e \sim 0.5$ eV is reached (Fig. 7f). At this temperature, the peak heat flux reaching the LFS divertor plate in the simulations is reduced to levels below 0.1 MW/m^2 (Fig. 7f). The peak LFS plate saturation current is reduced to about 20% below the peak value when the strike point electron temperature is reduced from 4 – 6 eV down to 1 eV, and further to about a factor 2 from the peak value when the 0.5 eV electron temperature levels are achieved. The lowest peak saturation current values obtained in the simulations were about a factor of 5 below the peak value and reached in the temperatures of about 0.25 eV. In divertor electron temperatures below 0.5 eV, volume recombination increases strongly with reducing electron temperature, and the electron density in front of the target rolls over. As a result, the LFS target pressure drops down to the range of a few % of the LFS mid-plane pressure. Simulations without 3-body and radiative recombination processes were not able to reach the roll over of the LFS target densities or LFS pressures lower than 10 – 20% of the mid-plane pressure (Figs. 7d – f). However, it is observed that omitting these volume recombination processes in the simulations, the target temperatures were also increased back to 0.5 eV, where significant density reduction was not observed even with the volume recombination processes included. Therefore, these volume recombination processes allow the plasma to enter a factor of 2 lower temperatures from 0.5

to 0.25 eV, which lead to a non-linear increase of the volume recombination sink once the processes are included in the simulations.

Even though there is little difference observed in the detachment characteristics for a given divertor electron temperature between the JET-C and JET-ILW PFCs, the simulations show that, for a given upstream electron collisionality, the electron temperatures in JET-C are up to a factor of 2 lower than those in JET-ILW (Fig. 8a). Therefore, the JET-C PFCs lead to lower peak electron temperatures at the LFS divertor plate resulting into about 10% lower peak and total saturation current roll over threshold for mid-plane electron density or collisionality (Figs. 8a, b, c, d). In the JET-C configuration, the simulations predict roll over of the peak saturation current at the LFS plate at about 30% lower electron collisionalities at the LFS mid-plane than the onset of strong volume recombination along this flux tube (ν_e ~ 3.3e17 $m^{-2}eV^{-2}$ vs. 4.5e17 $m^{-2}eV^{-2}$) (Fig. 8c, d). Similar results are obtained for the JET-ILW configuration (ν_e ~ 3.6e17 $m^{-2}eV^{-2}$ vs. 5.0e17 $m^{-2}eV^{-2}$). In the collisionality region above the onset of roll over of the $J_{SAT, LFS\text{-}target, peak}$ and below the onset of strong volume recombination along this flux tube, the $J_{SAT, LFS\text{-}target, peak}$ is reduced by about 30% in both wall configurations compared to maximum value preceding roll over. Therefore, as collisionality is increased and as LFS target electron temperatures decreases, the roll-over of $J_{SAT,LFS\text{-}target, peak}$ occurs before volume recombination is significant. Furthermore, before volume recombination becomes significant, $q_{LFS\text{-}target, peak}$ has already been reduced by about an order of magnitude relative to the levels obtained in the low collisionality, low recycling plasmas. In the collisionality region above the onset of strong volume recombination, the $J_{SAT, LFS\text{-}target, peak}$ is reduced by up to a factor of 4 in both configurations compared to the maximum value preceding roll-over. Volume recombination is an essential physics process providing access to this latter, deeply detached state. For the collisionality region preceding the onset of deep detachment, the reduction of $J_{SAT, LFS\text{-}target, peak}$ is provided dominantly by other processes than volume recombination. If the volume recombination processes are turned off in the simulations, the total and peak saturation current values in these deeply detached simulations increase back to the levels observed in the collisionality region preceding the onset of strong volume recombination.

The simulations show that in pure deuterium conditions the electron temperature at the LFS plate in JET-C relative to JET-ILW is reduced (1) due to reduced recycling levels at the strike point caused by stronger reflectivity in JET-ILW, thereby leading to hotter and sparser

plasma conditions locally in front of the strike point when compared to JET-C, similar to observations documented in [19], (2) due to 10 – 20% higher LFS divertor peak power deposition in JET-ILW relative to JET-C in high recycling conditions caused by reduced heat dissipation by molecular interaction (Fig. 8f), and (3) due to stronger energy reflectivity in JET-ILW therefore heating the divertor plasma relative to JET-C simulations similar to observations documented in [19]. The peak heat flux entering the LFS divertor is equal in the simulation between the two configurations. Furthermore, it is observed that due to these effects, at the LFS mid-plane electron collisionalities corresponding to the high-recycling LFS divertor regime, the peak LFS saturation current is up to a factor of 2 higher in JET-C than in JET-ILW. This is in qualitatively agreement with experimental observations (Figs. 2c, e). The impact of the changes in the divertor molecular density on the simulated deuterium radiation is less than 5 – 10% (Figs. 8f).

Due to stronger atomic reflectivity of the tungsten compared to carbon, the simulated atomic deuterium neutral pressures in the private flux region (PFR) can be up to a factor of 2 higher in JET-ILW than in JET-C, for a given LFS mid-plane collisionality (Fig. 9). Similar molecular deuterium pressures are predicted for the two wall configurations. Experimentally, similar sub divertor pressures were reported for JET-C and JET-ILW H-modes in similar conditions [5]. Similar findings were reported also for L-mode plasmas in JET [9].

b. Impact of carbon and beryllium radiation on the divertor conditions in the unseeded plasmas

i) The impact of carbon and beryllium on divertor radiation

Consistent with the experimental observations, a factor of 2 – 3 reduction in the radiated power in the divertor chamber is predicted with the change from JET-C to JET-ILW (Fig. 11a). Deuterium radiation is predicted to increase by 10 – 20% for a given upstream density when changing from JET-C to JET-ILW, whereas radiation by intrinsic impurities is reduced by up to 90%. This is due to a factor of 3 – 6 lower effective, total, non-coronal radiative potential of beryllium impurities when compared to carbon impurities in the simulations (Fig. 10). As a result, in the unseeded JET-ILW plasmas, deuterium provides about 90% of the divertor radiation, while in the unseeded JET-C simulations, deuterium contributes 40% to the total divertor radiation with carbon providing the remaining 60% in the base case simulations with a factor of 2 enhancement of the chemical sputtering yield. In the JET-ILW simulations, even assuming full beryllium divertor targets, the total beryllium

radiation in the computational domain increases only by a factor of 2, and the resulting beryllium radiation remains on levels less than 20% of the deuterium radiation in the plasmas. Furthermore, such an assumption is an extreme sensitivity study in contrast with experimental observations showing only little beryllium deposition on most of the divertor tiles in JET-ILW [52].

Sensitivity studies with carbon sputtering yield were conducted to artificially increase the carbon erosion source until the radiated power measured experimentally was reproduced by the simulations. These sensitivity studies resulted into a very large enhancement factor of 30 being necessary for the carbon sputtering yield. The high enhancement factors required here are presumably partially caused by omission of cross-field drifts and, as a result, underestimation of the HFS divertor densities and carbon erosion levels. Furthermore, omission of ELMs in the simulations is expected to lead to underestimation of the time averaged carbon erosion in the divertor. However, these simulations are used to investigate the sensitivity of the plasma solution to an artificially imposed carbon level in the background plasma. If the chemical sputtering yield of carbon is enhanced by a factor of 30, more than 90% of the total radiation is provided by carbon (Figs. 11a, b). However, these simulations overestimate the experimentally measured LFS divertor CIII (465 nm) emissions by a factor of 2 – 3 indicating that the carbon content in the divertor plasma is overestimated, therefore, compensating a short fall of radiated power by deuterium in the simulations (Fig. 11b). Also in previous JET-C simulations for these discharges high chemical sputtering yields required at the HFS target [13]. More previous studies investigating the impact of carbon sources and erosion yields on the plasma conditions can be found in [53 – 56, and references therein].

The density scan in the JET-ILW simulations spans the range of the experimentally measured divertor radiation values (Fig. 11a). However, in the simulation that provides the best representation of the LFS divertor conditions in the unseeded JET-ILW case (Figs. 12c – d), the total divertor radiated power is underestimated by a factor of 2. Therefore, similar to L-mode studies in JET [9], in both JET-ILW and JET-C the simulations under-predict the total divertor radiated power, whereas in JET-C this can be partially compensated by increasing the chemical sputtering yield, similar to studies documented in [13] (Figs. 11a, 12b). Nevertheless, comparisons of the divertor radiation distributions indicate that in the JET-ILW plasmas, the LFS divertor radiation values are underestimated by 10 – 25% only (fig. 12d). This indicates that in the unseeded JET-ILW H-mode plasmas, deuterium is indeed the dominant radiator, while the total radiation is presumably underestimated due to neglect of

cross-field drifts and the associated underestimation of the inner divertor densities and radiation, or due to other unaccounted physics processes. However, L-mode simulations in JET-ILW indicate that the impact of cross-field drifts on the total radiated power is significant only in low-density plasmas, where the radial temperature gradients and resulting **E**x**B**-drive are strong enough to enhance the in-out –asymmetries significantly [45]. In high density conditions, the simulations are likely to underestimate the total radiated power due to missing recombination and/or molecular interaction contributions, or other, unaccounted physics processes.

The electron cooling potential due to photonic radiation in the simulations, including the transport induced enhancement over the coronal levels, indicate that, as expected, the peak beryllium radiation occurs at around electron temperatures about 2 – 3 eV, whereas the peak carbon radiation occurs at around 10 – 30 eV (Fig. 10). Furthermore, it is observed that carbon can reach a factor of 2 – 3 higher peak radiative potential than beryllium in the simulations. Comparison to coronal equilibrium values indicate that the transport induced non-coronal effects in EDGE2D-EIRENE increase the effective radiative potential of beryllium by 2 – 3 orders of magnitude in the electron temperatures of 5 – 30 eV. 1 – 2 orders of magnitude enhancement is observed for carbon in the electron temperature range of 20 – 50 eV. It is also observed that there is significant scatter in the radiative potential of beryllium in the electron temperature range of 10 – 30 eV. This is presumably caused by two overlapping radiation regions. The first envelope is provided by the main chamber beryllium sputtering source in the simulations providing a direct source of low charge state beryllium to upstream plasmas in the temperatures in the range of tens of eVs, whereas the second envelope is caused by beryllium transported into the divertor plasma, thereby, having had sufficient time to ionize to higher charge states lowering the effective raditative potential. In electron temperatures about 30 – 100 eV, similar radiative potentials are predicted for carbon and beryllium impurities in the simulations. In electron temperatures above 100 eV, corresponding to the computational domain inside the separatrix, the radiative potential for both impurities are at low levels, therefore yielding less than 10% of the total radiation to occur inside the separatrix.

ii) The impact of carbon and beryllium on divertor power deposition

Consistent with the previous studies in L-mode plasmas, due to the reduced radiation levels in JET-ILW compared to JET-C, as well as due to the reduced power dissipation by

molecular interaction, the predicted outer divertor peak power and total power deposition is increased by 25 – 50% for a given LFS mid-plane electron density (Fig. 11c, d) [9]. The peak heat flux entering the LFS divertor is within 10% between the wall configurations for a given collisionality. When comparing to the JET-C simulations with the chemical sputtering enhanced by a factor of 30, the predicted divertor power deposition is higher in JET-ILW by a factor of 2 – 4. Consistently, the experimental measurements indicate 20 – 50% lower LFS power deposition values in JET-C than in JET-ILW. In JET-C, the experimental measurements indicate LFS divertor power deposition values about 1.5 – 3.5 MW, reducing with increasing deuterium fuelling [14]. In JET-ILW, for the highest achieved deuterium fuelling levels, 2.8 – 3e22/s, values about a factor of 2 higher, 3 – 4 MW, were measured for the unseeded plasmas than in JET-C. These values are also inline with the numbers obtained in the simulations (Fig. 11c). Also, the predicted peak heat fluxes at the LFS plate span the range of the experimental measurements, expect at the lowest electron collisionalities in JET-C (Fig. 11d, Fig. 9 in [14] and Fig. 9b in [6]). For the lowest electron collisionalities, the IRTV measures LFS peak heat fluxes in the range of 15 MW/m^2, whereas the simulations do not exceed the value of 7 MW/m^2 at the low collisionalities, which already represent sheath-limited plasma solutions. The measured peak heat fluxes can be reproduced by reducing the near SOL heat conductivity in the simulations to the levels used in ref. [13]. However, a large part of the peak heat flux in the low collisionality plasmas is presumably caused by direct neo-classical ion orbit loss particles, which cannot be properly represented by the fluid code [57, 58]. As a result, adjusting the radial transport coefficients in order to reproduce the peak heat fluxes in these conditions has a tendency to lead to overestimated divertor electron temperatures, since the power exhausted with ion-orbit loss particle in the experiment is channelled into the electron power exhaust channel in the fluid code [13, 58]. In the JET-C H-modes, the peak heat load between ELMs on the LFS target was strongly reduced by fuelling only [27]. Consistently with previous EDGE2D-EIRENE simulation, these studies indicate that a large fraction of this reduction is due to enhanced chemical sputtering of carbon and hence radiated power losses [13].

iii) The impact of carbon and beryllium on divertor conditions

As a result of the lower power deposition at the LFS divertor plate, up to a factor of 4 lower LFS divertor peak electron temperature is predicted for JET-C relative to JET-ILW for a given LFS mid-plane electron collisionality, consistent within the scatter of the experimental data (fig. 2c, 11e). Therefore, the LFS detachment threshold in electron

collisionality is predicted to be about 10 – 20% lower in JET-C than in JET-ILW (Fig. 11f). The peak heat flux at the LFS plate at the onset of detachment is about 0.5 – 0.8 MW/m^2 in these simulations, similar to the observations in the pure deuterium simulations in the previous section in this paper.

It was observed experimentally that in the unseeded plasmas for a given deuterium fuelling rate, the LFS divertor leg in the JET-ILW plasmas was in a low-radiation, low-recycling regime, whereas high recycling conditions were observed in the JET-C (Figs. 2c, e). This phenomenon is also seen in the simulations (Figs. 11e, f, Fig. 12). It is observed that for an upstream electron collisionality of about 2e17 m^{-2}eV^{-2}, the peak saturation current in the base case JET-C simulations exceeds the peak saturation current in the JET-ILW simulation by a factor of 1.5. A large part of this enhancement is caused by the lower deuterium reflectivity at the strike point with carbon PFCs, enhancing atomic and molecular deuterium density in front of the strike point, thus increasing the recycling levels and reducing the electron temperatures locally. Furthermore, the enhanced divertor radiation with carbon PFCs reduces the divertor temperatures leading to higher recycling divertor conditions. This latter phenomenon is further amplified in the simulations with the enhanced chemical sputtering of carbon (Fig. 12).

The JET-ILW simulations show a secondary peak in the LFS saturation current profile in the far SOL (Fig. 12c). This secondary peak is caused by the vertical transition between the JET divertor tiles 5 and 6, which is manifested as a step in the numerical grid. This corner generates a locally enhanced recycling zone on the tile 6. Based on the divertor Langmuir probe data it cannot be concluded whether this formation is physical or not, since the divertor Langmuir probes used for generating the saturation current profiles during the strike point sweeps are located on top of the tile 5. This formation is observed only in the JET-ILW simulations due to stronger reflectivity of the PFC components around the strike point producing higher amounts of fast reflective deuterium atoms, which recycle in the far SOL in this open horizontal divertor configuration. As a result, the divertor saturation current profile is on average wider and flatter in JET-ILW than in JET-C in the simulations and is, therefore, prone to occurrence of secondary peaks if there are corners or steps in the divertor target contours.

For the simulation case represented in Figure 12, the total LFS divertor D_α emission in this JET-ILW simulation is underestimated by a factor 2. The experimental LFS divertor D_α

emission can be reproduced by increasing the upstream electron density by 15 %. However, this leads to overestimation of the LFS divertor saturation currents by 40%. This finding is also consistent with generally underestimated deuterium radiation levels in the simulations. In other words, the total neutral deuterium recycling rates, i.e., divertor currents, and the total deuterium photon emission rates are challenging to be reproduced simultaneously in the simulations.

c. Impact of nitrogen seeding on the divertor conditions in JET-C and JET-ILW

i) Impact of nitrogen injection on the radiative properties of the JET-C and JET-ILW plasmas

Nitrogen is observed to entail radiative properties close to those of carbon in the simulations (Fig. 13). As expected, the peak radiative potential of carbon and nitrogen occurs at 10 – 30 eV, when including the transport-induced enhancement over the coronal equilibrium values, as given by EDGE2D-EIRENE. The peak radiative potential of nitrogen with the ADAS 96 dataset is roughly 10 % lower than that of carbon. Comparison to coronal equilibrium values indicate that the transport induced equilibrium effects in EDGE2D-EIRENE increase the effective radiative potential of nitrogen and carbon by 1 – 2 orders of magnitude in the electron temperatures of 20 – 50 eV. In electron temperatures about 40 – 100 eV, similar radiative potentials are predicted for carbon and nitrogen impurities in the simulations. In electron temperatures above 100 eV, corresponding to the computational domain inside the separatrix, the radiative potential for both impurities are at low levels, therefore yielding less than 20% of the total radiation to occur inside the simulations, as long as the simulations do not enter a radiation-condensation instability (MARFE-like formation) inside the X-point. Due to these reasons, both nitrogen and carbon are good divertor radiators for typical JET divertor conditions with electron temperatures in the range of 30 eV. Only the JET-ILW simulations did reach a transition to an energetically stable radiation-condensation (MARFE) formation inside the separatrix with X-point electron temperatures around 1 eV and electron densities about 1.3e21 m^{-3}. However, these simulations do not reach convergence, since the plasma solver diverges for these cases unless unacceptably small time steps (1e-9s) are employed. Furthermore, the credibility of these solutions is also compromised by omission of L_α opacity in these simulations [59]. Nevertheless, in such a formation, majority of the total radiation (~ 50 – 70 %) occurs inside the separatrix in the simulations.

With increasing nitrogen seeding, nitrogen radiation is predicted to increase in both

JET-C and JET-ILW, whereas the radiation due to deuterium and intrinsic impurities are predicted to reduce. The reduction of deuterium radiation is caused by reduced overall deuterium recycling rate in the simulations with increasing nitrogen seeding, whereas the reduction of beryllium and carbon radiation occurs due to reduced sputtering rate of these impurities. Consistently, experimentally, charge-exchange recombination spectroscopy also indicates substitution of intrinsic carbon with extrinsic species [60]. At the radiation levels required for detachment, in JET-ILW nitrogen provides about 87 %, deuterium about 9 %, and beryllium about 4 % of the total radiation. In the JET-C simulations, the breakdown is 73 % due to nitrogen, 18 % due to carbon and 9 % due to deuterium. Therefore, the missing carbon radiation in the JET-ILW environment is compensated by stronger nitrogen radiation contribution such that the LFS divertor detachment is imposed at similar divertor radiation values in both JET-C and JET-ILW, when imposing the divertor radiation with nitrogen, consistent with experimental observations.

ii) Impact of nitrogen on the divertor conditions, detachment and radiation distribution

Similar to experimental observations, the predicted LFS divertor peak heat flux is reduced nearly linearly from the unseeded levels of 3 – 5 MW/m^2 down to levels below 0.5 MW/m^2 when the divertor radiation levels increase from the unseeded 1 – 2 MW (~ 15 – 25% of P_{Sol}) levels to the 4 MW (~ 50% of P_{SOL}) levels corresponding to detached solutions (Fig. 14a). When imposing the divertor radiation with nitrogen injection in the simulations, it is observed that for a given divertor radiation, the peak and total heat flux at the LFS plate in JET-C is predicted to be about 20% lower than in JET-ILW. The peak heat flux entering the LFS divertor are the same within 10% for equal divertor radiated power values between the configurations. This is due to the extra heat dissipation by the molecular dissociation and collision processes in JET-C, which do not manifest themselves in the simulated radiated power. Experimentally, the data does not, however, allow discrimination, whether the LFS divertor power load for JET-C is lower than for JET-ILW for a given divertor radiation. Whereas in the unseeded simulations the peak LFS divertor heat flux is 30% lower in JET-C than in JET-ILW, with increasing nitrogen injection rate, the JET-ILW simulations reach the divertor radiation values and peak LFS heat fluxes predicted for the JET-C plasmas, consistent with experimental observations. With further nitrogen injection, the divertor radiation values are increased and the peak LFS fluxes reduced in both JET-C and JET-ILW simulations, such that the 0.5 MW/m^2 levels, required for detachment, are reached in both

configurations at around divertor radiated powers of 4 MW corresponding to roughly 50% of power crossing the separatrix, in these plasmas for heating powers of 15 – 17 (fig. 14a, b). The JET-C simulations reach this value at about 5% lower divertor radiated values than the JET-ILW simulations.

Similar to experimental observations, detachment induced by nitrogen occurs in both JET-C and JET-ILW simulations when the divertor radiated power reaches the levels of about 45 – 50% of the power crossing the separatrix, corresponding to divertor radiated power about 3.5 – 4 MW. This is indicated by reduction of the peak and total integral saturation current at the LFS divertor plate (Figs. 14b, c). In both the JET-ILW and the JET-C simulations, the total integral saturation currents begins to roll-over at about 0.5 MW lower divertor radiation values than the peak saturation current at the plate. In this phase, the far SOL LFS target particle fluxes begin to reduce, whereas little reduction is observed in the strike-point saturation current. Once the LFS peak heat flux is reduced below 0.5 MW/m^2, the onset of strike point detachment occurs in the simulation (Figs. 14a, b). The peak LFS divertor radiation front is shifted from the divertor leg to the LFS SOL X-point following the onset of strike point detachment in both JET-C and JET-ILW simulations, similar to experimental observations. In these divertor conditions, the LFS divertor leg electron temperatures drop below 5 eV, required for divertor detachment to occur. This also reduces the radiative potential of nitrogen and carbon in the divertor leg (Fig. 13). As a result, the peak radiation front shifts to the LFS X-point, where the cross-field heat source from the confined region and the shallow magnetic pitch angle enable the SOL plasma to maintain the electron temperatures sufficiently high for impurity radiation.

Similar detachment threshold peak LFS target heat flux values of 0.5 MW/m^2 are observed in the simulated seeded, unseeded and pure deuterium plasmas (Figs. 7f, 11d, 14a). In these conditions, in the seeded simulations, about 60% of the peak heat flux in the simulations is provided by particle recombination at the target and only 40% (0.2 MW/m^2) via plasma transport. Surface heating due to neutral particles and photonic radiation are not taken into account in the calculations, and the surface recombination model assumes only 13.6 eV energy release per an ion-electron pair depositing on the target surface neglecting the 2.2 eV energy released per molecular recombination.

The peak saturation current values prior to detachment are underestimated by a factor of 1.5 – 2 in both the JET-C and JET-ILW simulations (Fig. 14b). This is similar to findings

published in [15], where it was observed that assuming full recycling for nitrogen, the peak saturation current at the LFS plate was underestimated by the same amount, whereas with zero recycling assumption for nitrogen, the peak saturation current prior to detachment was reproduced within the experimental error bars. Basically, it was observed that the plasma conditions at the LFS divertor target are sensitive to the nitrogen source distribution close to the injection valve, and neither full or zero recycling assumption is expected to capture the details of this source distribution appropriately. However, the zero nitrogen recycling simulations fail to reproduce the global radiation distribution in the plasma, which is why the full recycling assumption was chosen for this study.

Both in the JET-C and JET-ILW simulations, with increasing nitrogen seeding and impurity radiation, the $J_{SAT,LFS\text{-}target,peak}$ rolls over before the onset of strong volume recombination in the divertor. At the point of sharp reduction of $J_{SAT,LFS\text{-}target,peak}$, the $q_{LFS,peak}$ is already reduced by an order of magnitude relative to the unseeded values, and the peak $T_{e,LFS}$ at the plate is less than 2 eV. In an impurity radiation induced detachment, an additional process providing divertor particle flux reduction, in addition to the processes observed in the detachment with deuterium fuelling only, is reduction of the overall deuterium recycling rate in the divertor leg, as was published in [15] (Fig. 14c). The reduced recycling rate is possible due to strong extrinsic impurity radiation reducing the power flow reaching the deuterium ionization front, thereby, reducing the total deuterium ionization rate. Together with sufficient momentum losses in the low field side divertor leg limiting the plasma flow to the target and volume recombination region, the overall recycling rate is reduced in these simulations. The overall momentum losses in the LFS divertor leg due to neutral interaction in these simulations reach values comparable to the total hydrodynamic pressure of the SOL plasma above the X-point.

In steady-state simulations, the density in the divertor leg does increase with reducing temperatures in the impurity radiation induced detachment as is observed in the Stark broadening profile in Figure 6. However, the recombination sink in front of the targets does not reach high enough values in steady-state simulations in this study for the volumetric electron density to reduce significantly in front of the target. A strong recombination sink in front of the target is reached in the model if nitrogen is allowed to radiate in temperatures lower than 0.3 eV in the model. However, the onset of this recombination sink in the model leads to an abrupt and strong recombination runaway in the solution such that the volumetric temperatures in the model drop all the way down to the lower limit value in the code (0.05

eV) and the plasma solution diverges, therefore, preventing achievement of converging solutions in these conditions. Therefore, to achieve a converging solution for these plasmas, the nitrogen radiation was limited in the model to regions with electron temperatures above 0.3 eV. Furthermore, it is a matter of debate whether the recombination runaway observed in the model when allowing nitrogen to radiate all the way down to 0.05 eV truly represents what is observed in the experiment.

The LFS divertor D_α emissions are underestimated by a factor of 2 in the unseeded Jet-ILW plasmas (Fig. 14d). With increasing nitrogen seeding, the LFS divertor D_α emissions is measured to increase reaching maximum values of roughly a factor of 2 – 3 higher than in the unseeded basecase. In contrast, with nitrogen seeding in the simulations, the D_α emission in the LFS divertor leg increases first slightly by about 30%, after which it is reduced with increasing nitrogen injection all the way until a strongly recombining solution is obtained (Fig. 14d). The discrepancy in the detached solutions is presumably caused by underestimated volume recombination in the simulations, therefore, underestimating the recombination D_α emission. In those simulations running into the recombination runaway, the divertor D_α emission reaches 1e17 ph/cm^{2}ssr levels in the LFS divertor leg. However, as was discussed in the previous paragraph, converged solution in such a state has not been obtained by the time of writing this report. Furthermore, the D_α emission is presumably underestimated also due to unaccounted emission by deuterium molecules and other unaccounted processes.

5. Conclusion

Highly shaped, high confinement mode plasmas in JET-C and JET-ILW with and without nitrogen seeding have been interpreted with the aid of EDGE2D-EIRENE simulations. Transition to detachment assisted by nitrogen at the LFS target plate is predicted and measured in both wall configurations when more than 45 – 50% of the power crossing the separatrix is radiated in the divertor, corresponding to divertor radiated power of about 4 MW. In these conditions LFS peak heat fluxes below 0.5 – 1 MW/m^2 are predicted and measured for both JET-ILW and JET-C. Following the change from JET-C to JET-ILW, a factor of 2 – 4 reduction in the divertor radiated power and 25 – 50% increase in the power deposited to the outer plate is predicted by EDGE2D-EIRENE for unseeded plasmas similar to experimental observations. This is attributed to a factor of 3 – 6 higher effective radiative potential of carbon compared to beryllium in the simulated divertor conditions. Furthermore, EDGE2D-EIRENE simulations indicate that the stronger molecular contribution in the

divertor recycling fluxes, in JET-C when compared to JET-ILW, reduces the divertor peak and total power deposition in high recycling conditions by 10 – 20% due to enhanced power dissipation by molecular interaction. Due to these processes, 10 – 20% lower peak and total saturation current roll over threshold in electron collisinality at the LFS mid-plane is predicted for the JET-C simulations than for the JET-ILW. At the detachment threshold, EDGE2D-EIRENE shows that nitrogen is radiating more than 80% of the total divertor radiation with the ITER-like wall with beryllium contributing less than a few %. With the carbon wall, nitrogen radiation contribution is more than 70% with carbon providing less than 20% of the total radiation. Therefore, the lower intrinsic divertor radiation with the ITER-like wall is compensated by stronger nitrogen radiation in the simulations leading to detachment at similar total divertor radiation fractions, when imposing the divertor radiation with nitrogen. The LFS divertor D_α emission is measured to increase by a factor of 2 – 3 in the nitrogen induced detachment in JET-ILW. While the simulations underestimate the D_α emission throughout the seeding scan, a strong increase in the divertor D_α emission in the simulations is observed only after the onset of strong recombination sink in the divertor leg.

This work has been carried out within the framework of the EUROfusion Consortium and has received funding from the Euratom research and training programme 2014-2018 under grant agreement No 633053. The views and opinions expressed herein do not necessarily reflect those of the European Commission.

[1] KALLENBACH, A. et al., Plasma Phys. Control. Fusion **55** (2013) 124041

[2] MATTHEWS, G.F. et al., Phys. Scr. **T145** (2011) 014001

[3] BREZINSEK, S. et al., J. Nucl. Mater. **438** (2013) S303 – S308

[4] BREZINSEK, S. et al., Nucl. Fusion **53** (2013) 083023

[5] GIROUD, C. et al., Nucl. Fusion **53** (2013) 113025

[6] MADDISON, G. et al., Nucl. Fusion **54** (2014) 073016

[7] BEURSKENS, M.N.A. et al., Plasma Phys. Control. Fusion **55** (2013) 124043

[8] GIROUD, C. et al., Plasma Phys. Control. Fusion **57** (2015) 035004

[9] GROTH, M. et al., Nucl. Fusion **53** (2013) 093016

[10] SIMONINI, R. et al., Contrib. Plasma Phys. **34** (1994) 368 – 373

[11] REITER, D. J. Nucl. Mater. **196 – 198** (1992) 80 – 89

[12] WIESEN, S., ITC- Report,
http://www.eirene.de/e2deir_report_30jun06.pdf (2006)

[13] MOULTON, D. et al., J. Nucl. Mater. **415** (2011) S500 – S512

[14] GIROUD, C. et al., Nucl. Fusion **52** (2012) 063022

[15] JAERVINEN, A. et al., J. Nucl. Mater. **463** (2015) S135 – 142

[16] ECKSTEIN, W. Suppl. Nucl. Fusion **1** (1991) 17

[17] SERGIENKO, G. et al., J. Nucl. Mater. **438** (2013) S1100 – S1103

[18] JAERVINEN, A. et al., Proceedings of the 38th EPS Conference on Plasma Physics 2013

[19] BUFFERAND, H. et al., J. Nucl. Mater. **463** (2015) S420 – 423

[20] BEURSKENS, M.N.A. et al., Nucl. Fusion **48** (2008) 095004

[21] BRIX, M. et al., Rec. Sci. Instrum. **83** (2012) 10D533

[22] MONK, R.D. et al., J. Nucl. Mater. **241 – 243** (1997) 396

[23] MORGAN, P.D. et al., Rev. Sci. Instrum. **56** (1985) 862

[24] LOMANOWSKI, B.A. et al., Rev. Sci. Instrum. **85** (2014) 11E432

[25] HUBER, A. et al., Fusion Eng. Des. **82** (2007) 1327

[26] EICH, T. et al., J. Nucl. Mater. **415** (2011) S856

[27] MADDISON, G. et al., Nucl. Fusion **51** (2011) 042001

[28] LEYLAND, M.J. et al., Nucl. Fusion **53** (2013) 083028

[29] LEYLAND, M.J. et al., Nucl. Fusion **55** (2015) 013019

[30] ECKSTEIN, W. et al., Sputtering by particle Bombardment, Springer Publishing, (2007)

[31] ROTH, J. et al., J. Nucl. Mater. **337 – 339** (2005) 970 – 974

[32] SUMMERS, H.P. 1994 Atomic data and analysis structure users manual, JET-IR 06 (Abingdon:JET Joint Undertaking)

[33] JAERVINEN, A.E. et al., J. Nucl. Mater. **438** (2013) S1005 – S1009

[34] WIESEN, S. et al., Plasma Phys. Control. Fusion **53** (2011) 124039

[35] TSKHAKAYA, D. et al., J. Nucl. Mater. **463** (2015) S624 – 628

[36] JAERVINEN, A.E. et al., Phys. Scr. **T145** (2011) 014013

[37] OBERKOFLER, M. et al., J. Nucl. Mater. **438** (2013) S258 – S261

[38] KOTOV, V. et al., Plasma Phys. Control. Fusion **50** (2008) 105012

[39] GUILLEMAUT, C. et al., Nucl. Fusion, 54 (2014) 093012

[40] BOHM, D., The Characteristics of Electrical Discharges in Magnetic Fields, New York: McGraw-Hill, 1949,Press, 1986

[41] CHODURA, R., Physics of Plasma-Wall Interactions in Controlled Fusion, New York: Plenum Press, 1986

[42] STANGEBY, P.C., The Plasma Boundary of Magnetic Fusion Devices, IoP Publishing, 2000, ISBN 0-7503-0559-2

[43] CHANKIN, A. et al., Plasma Phys. Control. Fusion, **57** (2015) 9

[44] AHO-MANTILA, L. et al., "Assessment of Scrape-off Layer Simulations with Drifts against L-mode Experiments in ASDEX Upgrade and JET", [TH/3-3], paper presented at 25th IAEA Int. Conf. on Fusion Energy St Petersburg 2014

[45] GROTH, M. et al., "Steps in Validating Scrape-off Layer Simulations of Detached Plasmas in the JET ITER-like Wall Configuration", [TH/P-35], paper presented at 25th IAEA Int. Conf. on Fusion Energy St Petersburg 2014.

[46] HOLLMAN, E.M. et al., Plasma Phys. Control. Fusion **48** (2006) 1165 – 1180

[47] BREZINSEK, S. et al., Contrib. Plasma Phys. **42** (2002) 6 – 7, 668 – 674

[48] BREZINSEK, S. et al., J. Nucl. Mater. **463** (2015) S11 – 21

[49] KOTOV, V., REITER, D. and KUKUSHKIN, A.S., Report Jül-4257, www.eirene.de/kotov_solps42_report.pdf, 2007

[50] KUKUSHKIN, A.S. et al., Nucl. Fusion, **45** (2005) 608

[51] WISHCMEIER, M. et al., 2012 Proc. 24th Int. Conf. on Fusion Energy (San Diego, 2012) [EX/P5-34] http://www-naweb.iaea.org/napc/physics/FEC/FEC2012/index.htm

[52] WIDDOWSON, A. et al., Phys. Scr. **T159** (2014) 014010

[53] STRACHAN, J.D. et al., J. Nucl. Mater. **390 – 391** (2009) 92 – 95

[54] STRACHAN, J.*D.* et al., Nucl. Fusion **43** (2003) 922

[55] STRACHAN, J.D. et al., Nucl. Fusion **44** (2004) 772

[56] STRACHAN, J.D. et al., Nucl. Fusion **48** (2008) 105002

[57] FUNDAMENSKI, W. et al., Nucl. Fusion **45** (2005) 950 – 975

[58] KALLENBACH, A. et al., Plasma Phys. Control. Fusion **46** (2004) 431

[59] KOTOV, V. et al., Plasma Phys. Control. Fusion **54** (2012) 082003

[60] MADDISON, G. et al., J. Nucl. Mater **415** (2011) S313 – S317

Figure captions:

Figure 1. The poloidal magnetic equilibrium of the investigated JET plasmas. The main diagnostics used in this study are highlighted: a high resolution Thomson scattering system (HRTS [20], black line at the LFS mid-plane), a Lithium beam system (Li-beam [21], black at the top), an array of target Langmuir probes [22] (Magenta), and divertor visual spectroscopy systems [23, 24] (black, red, and blue). The total radiated power was measured with a multiple-chord bolometer and reconstructed tomographically [25]. A vertical viewing infrared thermography (not shown) was used to estimate the low-field side power deposition [26]. Deuterium was injected into the chamber at the HFS target, while nitrogen seeded at the LFS target into common SOL. The definitions of the macro-zones used for integrating the bolometric reconstructions for the LFS and HFS divertor regions are illustrated with dashed lines.

Figure 2. a) LFS mid-plane separatrix electron density, measured with the JET HRTS system, as a function of deuterium injection rates. The black circles represent JET-C plasmas and the red squares represent JET-ILW discharges. b) Radiated power in the LFS (solid symbols), $P_{RAD,\ LFS\text{-}DIV,\ integ.}$, and HFS (open symbols), $P_{RAD,\ HFS\text{-}DV,\ integ.}$, divertor chamber (vertical height below -1.2 m). c) Peak electron temperature at the LFS divertor plate, $T_{e,\ LFS\text{-}target,\ peak}$, as measured by the divertor Langmuir Probes. d) Peak saturation current at the LFS plate, $J_{SAT,\ LFS\text{-}target,\ peak}$. The error bars represent standard deviation of the investigated signals within 75 – 95% of the ELM-cycles in the flattop phase of the investigated discharge, except for the LFS mid-plane separatrix electron density an uncertainty of +/- 1e19 m^{-3} is assumed.

Figure 3. a) LFS mid-plane separatrix electron density, measured with the JET HRTS system, as a function divertor radiated power with nitrogen seeding. The black circles represent JET-C plasmas and the red squares represent JET-ILW discharges. b) Radiated power in the LFS (solid symbols), $P_{RAD,\ LFS\text{-}DIV,\ integ.}$, and HFS (open symbols)), $P_{RAD,\ HFS\text{-}DV,\ integ.}$, divertor chamber (vertical height below -1.2 m). c) Peak electron temperature at the LFS divertor plate, $T_{e,\ LFS\text{-}target,\ peak}$, as measured by the divertor Langmuir Probes. d) Peak saturation current at the LFS plate, $J_{SAT,\ LFS\text{-}target,\ peak}$. The error bars represent standard deviation of the investigated signals within 75 – 95% of the ELM-cycles in the flattop phase of the investigated discharge, except for the LFS mid-plane separatrix electron density an uncertainty of +/- 1e19 m^{-3} is assumed. The deuterium injection rate in the illustrated nitrogen seeded plasma was in the range of 1.5 – 2.8e22 e/s.

Figure 4. Reconstruction of the bolometric radiated power in the JET-C and JET-ILW with increasing N_2-injection rate for a D_2-injection rate of about 2.6 – 2.8e22 e/s. The upper row (a – d) represents the seeding scan in JET-ILW and the lower row represented the seeding scan in JET-C.

Figure 5. Line-integrated radiation as measured by the vertical bolometer channels spanning the divertor chamber in the JET-C and JET-ILW with increasing N_2-injection rate for a D_2 injection rate of about 2.6 – 2.8e22 e/s. The line of sight geometry is shown in the embedded figure in the figure a. The dashed line represents the location of the X-point relative to the line-of-sights. The HFS and LFS stand for high- and low-field-sides respectively. JET-C data-points are represented with solid circles and the JET-ILW data-points are represented with solid squares.

Figure 6. Stark broadening electron density profile, based on the JET spectroscopic system KT3, in the LFS divertor leg in a detached JET-ILW plasma with 16 MW of NBI heating and 3 MW of ICRH heating at deuterium fuelling rate of 2.8e22 e/s and nitrogen injection rate of 3.8e22 e/s.

Figure 7. The ion fraction of the total divertor recycling flux re-emitted as molecules (a), the fraction of the impinging energy reflected on the divertor targets (b), the ratio of the total molecular neutral deuterium density to the total neutral deuterium density in the divertor (c), the simulated total hydrodynamic pressure-ratio between the LFS strike point and the LFS mid-plane separatrix (d), the simulated LFS divertor peak saturation current, $J_{sat,\ LFS\text{-}target,\ peak}$ (e), and the simulated LFS target peak electron density, $n_{e,\ LFS\text{-}target,\ peak}$ (solid symbols) and peak heat flux, $q_{LFS\text{-}target,\ peak}$ (open symbols) (f) as a function of the strike point electron temperature at the LFS target plate. The red squares represent pure deuterium simulations with the JET-ILW configuration and the black symbols simulations with the JET-C configuration. The blue triangles in the figures d – f represent the JET-ILW simulations at the highest obtained separatrix density without 3-body and radiative volume recombination processes. The LFS target peak density in the simulation without volume recombination processes increases above the shown scale up to 1.7e21 m^{-3}. Log-linear relation between the molecular fraction in the divertor recycling and the peak electron temperature at the LFS divertor plate is observed and illustrated with the corresponding equations and trend-lines in the figure (a). The dashed lines in the figure (d) illustrate the 80%, 50%, 10% and 5% pressure-ratio levels.

Figure 8. The simulated LFS plate strike point electron temperature, $T_{e,strike\ point}$, (a), the simulated integrated LFS plate particle flux, $I_{LFS\text{-}target,\ integ.}$, the integrated LFS SOL deuterium ionization rate, $S_{IONIZ,\ LFS,\ SOL,\ integ.}$, the integrated LFS SOL deuterium recombination rate, $S_{RECOM,\ LFS,\ SOL,\ integ.}$ (b), the simulated LFS peak saturation current, $J_{SAT,\ LFS\text{-}target,\ peak}$, (c), the simulated near SOL LFS plate particle flux, $I_{LFS\text{-}target,\ near\ SOL}$, the near LFS SOL deuterium ionization rate, $S_{IONIZ,\ near\ SOL}$, the near LFS SOL deuterium recombination rate, $S_{RECOM,\ near\ SOL}$ (d), the simulated LFS plate peak power deposition, $q_{LFS\text{-}target,\ peak}$ (e), and the simulated deuterium radiation within the computational domain (solid symbols), and the energy loss due to molecular interaction (hollow symbols) (f), as a function of the LFS mid plane electron collisionality ($n_e L/T_e^2$). The near SOL stands here for SOL within 0.5 cm from the separatrix at the LFS mid-plane. The connection length is assumed to be 40 m, which is approximately the LFS target to LFS mid plane distance along the separatrix field line at JET. The symbols and colours are as in Fig. 7.

Figure 9. Simulated neutral pressure in the private flux region (PFR) in the pure deuterium simulations in JET-ILW (red) and JET-C (black). Only the region spanned by the computational grid of EDGE2D is included. The solid symbols represent atomic deuterium pressure and the hollow symbols the molecule pressure.

Figure 10. Simulated electron cooling power function due to photonic radiation caused by carbon (C) and beryllium (Be) in the base case simulations at outer mid-plane electron collisionality of 2e17 $m^{-2}eV^{-2}$ (circled black and red cases in Fig. 11f). The solid line represent the coronal equilibrium values calculated based on ADAS 96 rates. ADAS 96 are also used in the EDGE2D-EIRENE simulations.

Figure 11. The integrated simulated radiated power in the divertor chamber (Z < -1.2 m), $P_{Rad,\ DIV,\ integ.}$ (a), the integrated simulated CIII (465 nm) emission in the LFS divertor leg (b), the integrated simulated LFS plate power deposition, $P_{LFS\text{-}target,\ integ.}$ (c), the simulated LFS plate peak power flux, $q_{LFS\text{-}target,\ peak}$ (d), the simulated LFS plate strike point electron

temperature, $T_{e,\ LFS\text{-}target,\ strike\ point}$ (e), and the simulated LFS plate peak saturation current, $J_{SAT,\ LFS\text{-}target,\ peak}$ (f), as a function of the LFS mid-plane electron collisionality (n_eL/T_e^2). The connection length is assumed to be 40 m. The grey and red shading in the figure (a) represent the range of the experimentally measured values. The grey shading in the figure (b) represents the experimentally measured values with the JET divertor spectrometer KS3. The red symbols stand for JET-ILW simulations, the black symbols for the JET-C simulations with the chemical sputtering yield multiplied by a factor of 2 and the blue symbols for the JET-C simulations with the chemical sputtering yield multiplied by a factor of 30. The simulation cases further illustrated in Fig. 12 below are circled in Fig. f.

Figure 12. Comparison of the measured and predicted LFS plate saturation current profiles and vertical divertor line integrated radiated power values for JET-C (a, b), and JET-ILW (c, d) plasmas without seeding. The experimental data-points are obtained for the deuterium fuelling rate about 2.8e22 e/s. The simulation lines represent the simulations with LFS mid-plane electron collisionality of 2e17 $m^{-2}eV^{-2}$ in Fig. 11f. The color-coding is the similar to Fig. 11.

Figure 13. Simulated electron cooling power function due to photonic radiation caused by carbon (C, black), and nitrogen (N, red) in the simulations with about 3.5 MW of divertor radiation. The solid line represent the coronal equilibrium values calculated based on ADAS 96 atomic rates. The dots represent non-coronal values calculated by EDGE2D-EIRENE simulations.

Figure 14. LFS divertor target peak heat flux, $q_{LFS\text{-}target,\ peak}$, (a) LFS divertor peak saturation current, $J_{sat,\ LFS\text{-}target,\ peak}$, (b) and integrated LFS SOL total ionisation source, $S_{ionization,\ LFS,\ SOL,\ integ.}$ (upper hollow symbols), integrated LFS divertor target particle flux, $I_{LFS\text{-}target,\ integ.}$ (solid symbols), and integrated total LFS SOL recombination sink, $S_{recombination,\ LFS,\ SOL,\ integ.}$ (lower hollow symbols) in the seeded JET-ILW (red) and the JET-C (black) simulations, as a function of the total divertor radiated power below Z = -1.2 m. d) Measured and predicted integrated LFS divertor D_α emission. The hollow red squares and the hollow black circles in Figs. a and b represent experimental data points in the JET-ILW and JET-C environments, respectively. The red lines represent EDGE2D-EIRENE simulations with the JET-ILW material configuration and the black lines simulations with the JET-C material configuration.

Figure 1.

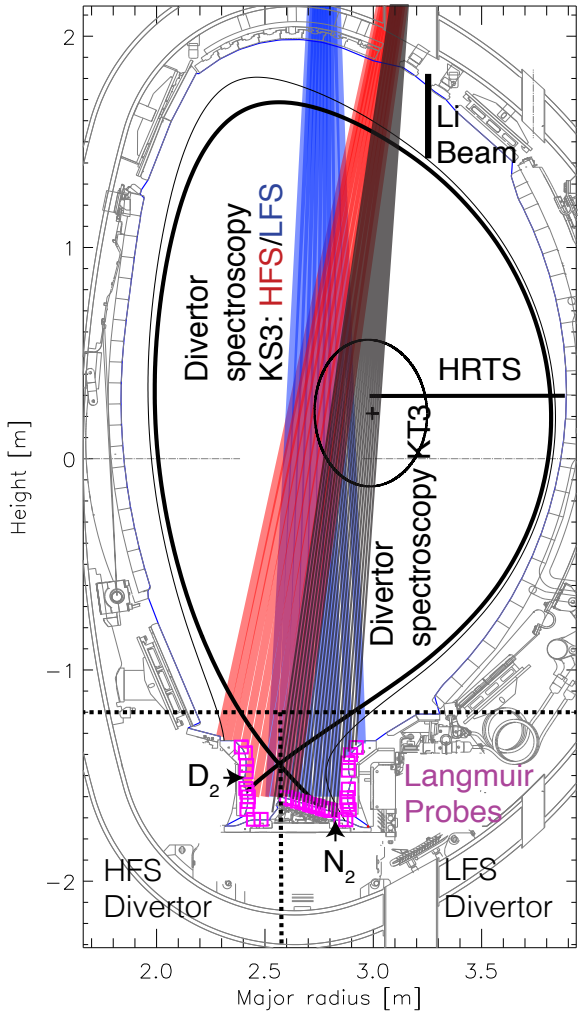
Li
Beam
Divertor
spectroscopy
KS3: HFS/LFS
HRTS
Divertor spectroscopy KT3
D2
N2
Langmuir
Probes
HFS
Divertor
LFS
Divertor
Height [m]
Major radius [m]
2
1
0
−1
−2
2.0
2.5
3.0
3.5

Figure 2.

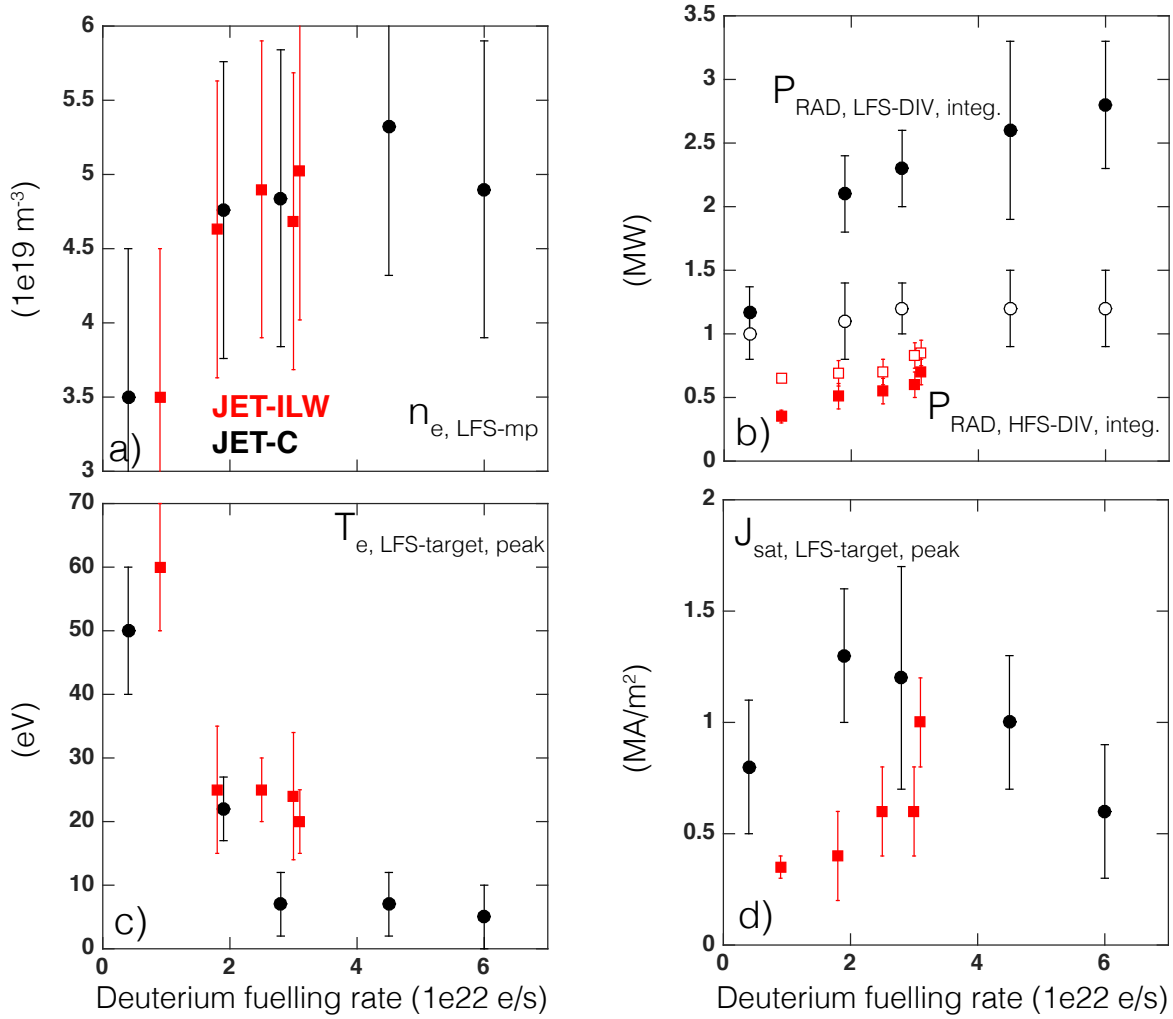
(1e19 m-3)
JET-ILW
JET-C
a)
ne, LFS-mp
(MW)
PRAD, LFS-DIV, integ.
b)
PRAD, HFS-DIV, integ.
(eV)
Te, LFS-target, peak
c)
(MA/m2)
Jsat, LFS-target, peak
d)
Deuterium fuelling rate (1e22 e/s)
Deuterium fuelling rate (1e22 e/s)

Figure 3.

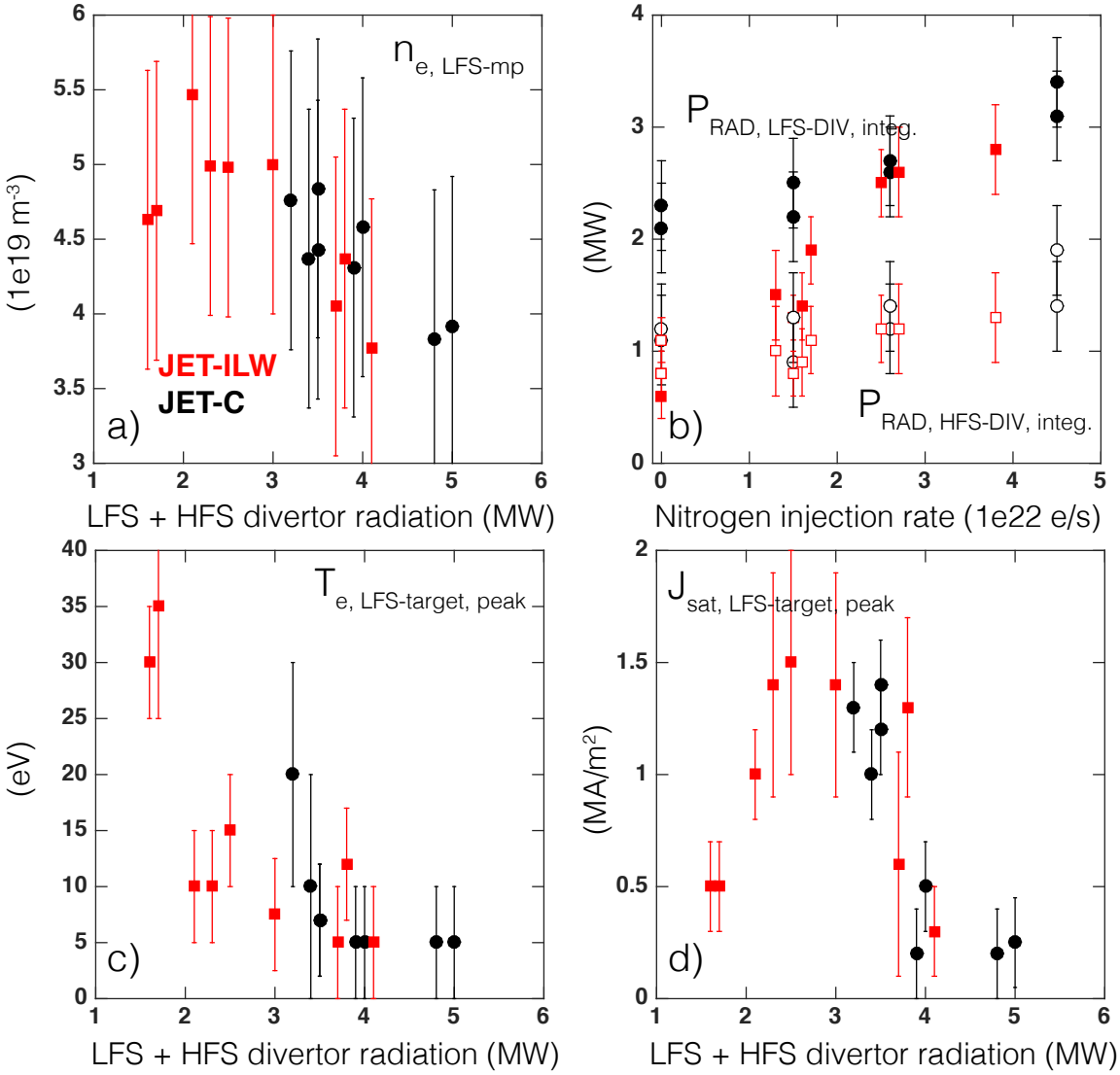

Figure 4.

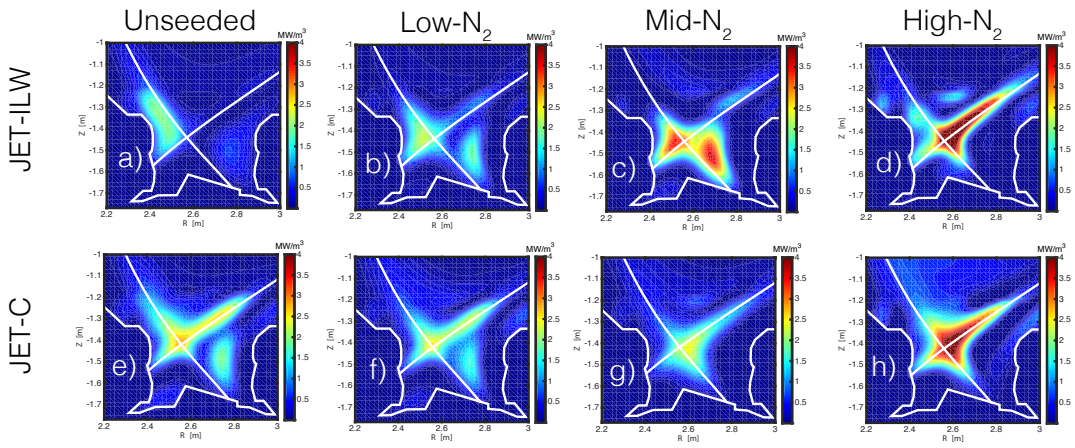
Unseeded
Low-N2
Mid-N2
High-N2
JET-ILW
JET-C
a)
b)
c)
d)
e)
f)
g)
h)
MW/m3
R [m]
Z [m]

Figure 5.

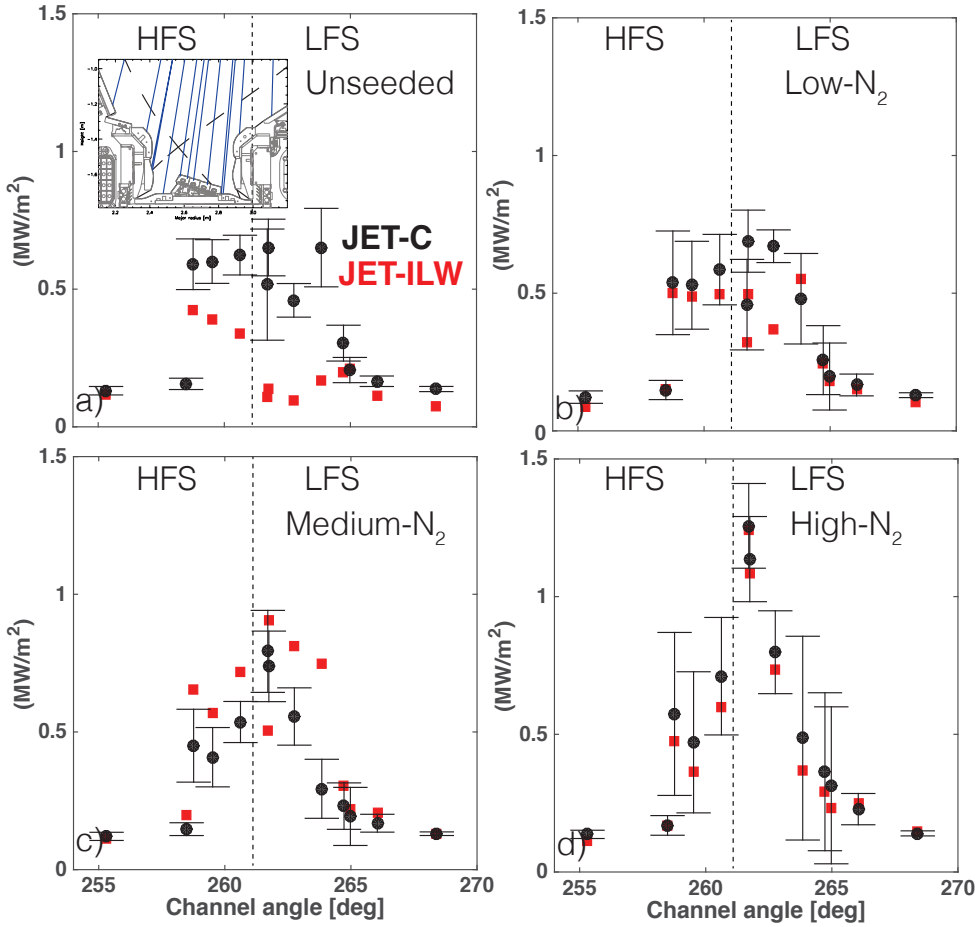
HFS
LFS
Unseeded
JET-C
JET-ILW
a)
HFS
LFS
Low-N2
b)
HFS
LFS
Medium-N2
c)
HFS
LFS
High-N2
d)
(MW/m2)
1.5
1
0.5
0
255
260
265
270
Channel angle [deg]

Figure 6.

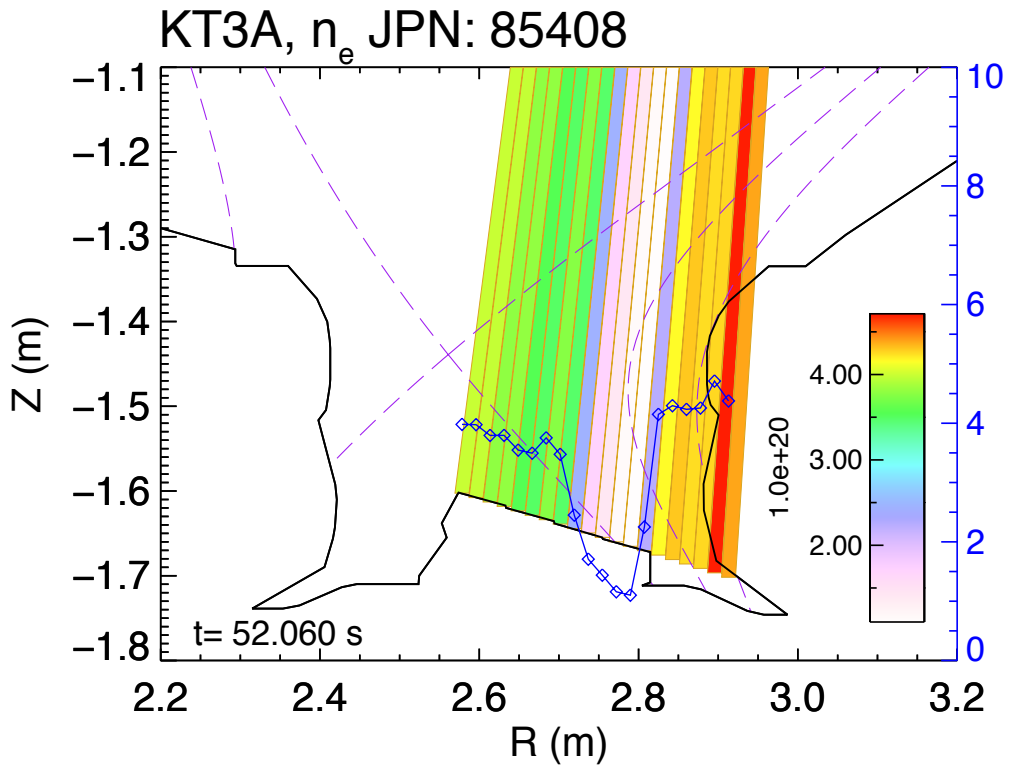
KT3A, n_e JPN: 85408
Z (m)
R (m)
t= 52.060 s
1.0e+20
4.00
3.00
2.00
−1.1
−1.2
−1.3
−1.4
−1.5
−1.6
−1.7
−1.8
2.2
2.4
2.6
2.8
3.0
3.2
10
8
6
4
2
0

Figure 7.

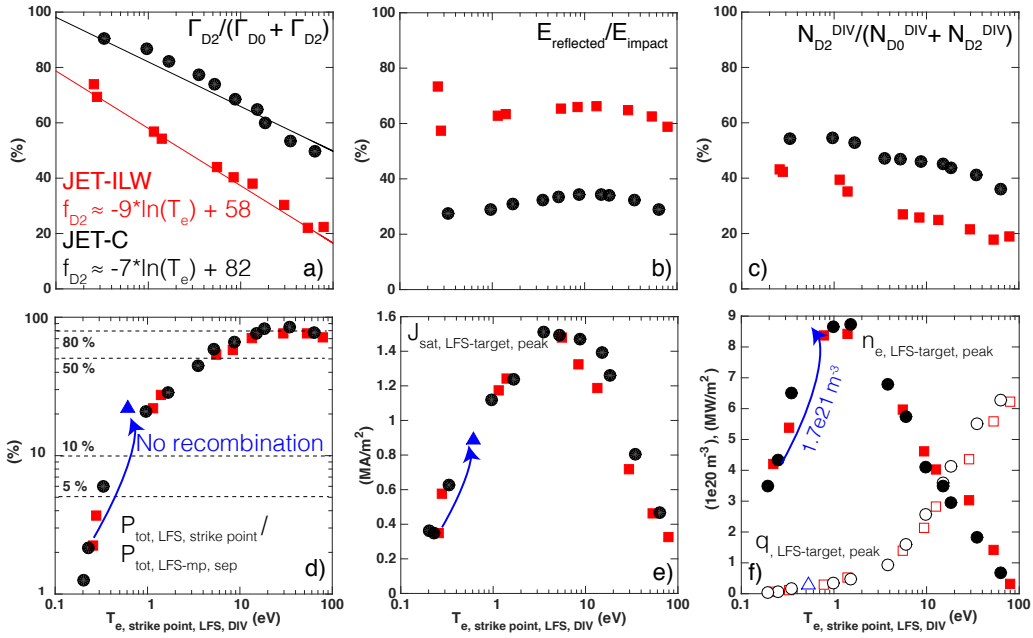
Γ_D2/(Γ_D0 + Γ_D2)
JET-ILW
f_D2 ≈ -9*ln(T_e) + 58
JET-C
f_D2 ≈ -7*ln(T_e) + 82
a)
E_reflected/E_impact
b)
N_D2^DIV/(N_D0^DIV + N_D2^DIV)
c)
80 %
50 %
10 %
5 %
No recombination
P_tot, LFS, strike point / P_tot, LFS-mp, sep
d)
J_sat, LFS-target, peak
e)
n_e, LFS-target, peak
1.7e21 m^-3
q_, LFS-target, peak
f)
(%)
(MA/m^2)
(1e20 m^-3), (MW/m^2)
T_e, strike point, LFS, DIV (eV)

Figure 8.

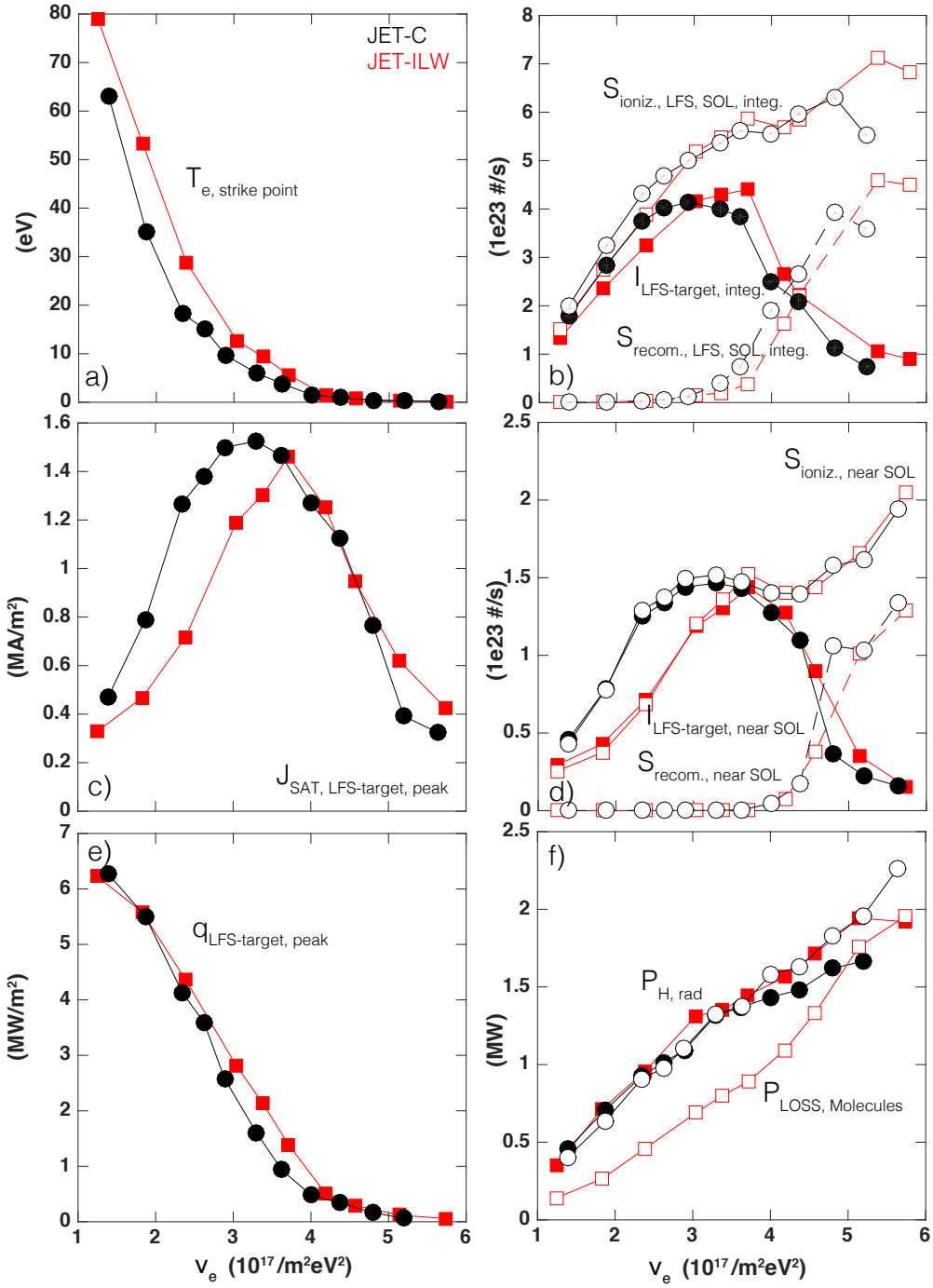
JET-C
JET-ILW
T e, strike point
(eV)
a)
S ioniz., LFS, SOL, integ.
I LFS-target, integ.
S recom., LFS, SOL, integ.
(1e23 #/s)
b)
J SAT, LFS-target, peak
(MA/m²)
c)
S ioniz., near SOL
I LFS-target, near SOL
S recom., near SOL
(1e23 #/s)
d)
q LFS-target, peak
(MW/m²)
e)
P H, rad
P LOSS, Molecules
(MW)
f)
v e (10¹⁷/m²eV²)
v e (10¹⁷/m²eV²)

Figure 9.

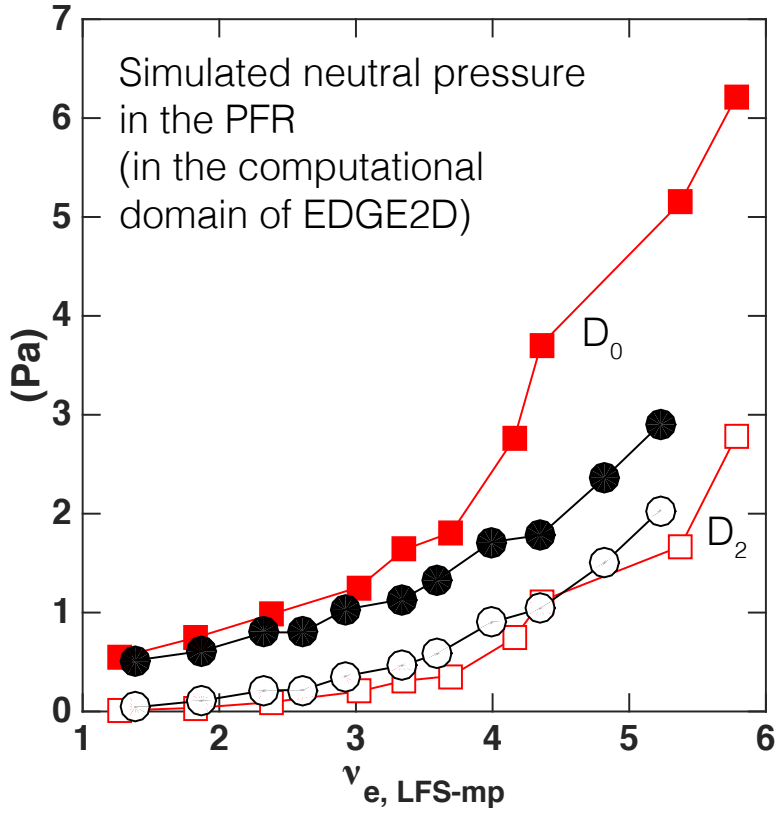
Simulated neutral pressure
in the PFR
(in the computational
domain of EDGE2D)
D0
D2
(Pa)
0
1
2
3
4
5
6
7
1
2
3
4
5
6
νe, LFS-mp

Figure 10.

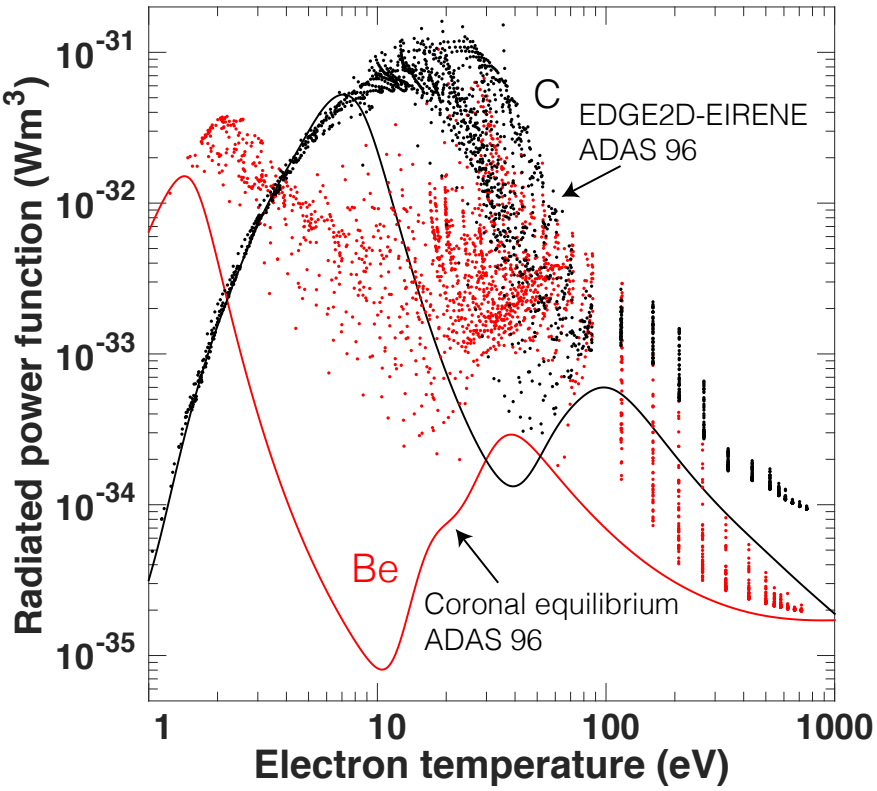
Radiated power function (Wm^3)
10^{-31}
10^{-32}
10^{-33}
10^{-34}
10^{-35}
1
10
100
1000
Electron temperature (eV)
C
EDGE2D-EIRENE
ADAS 96
Be
Coronal equilibrium
ADAS 96

1

Figure 11.

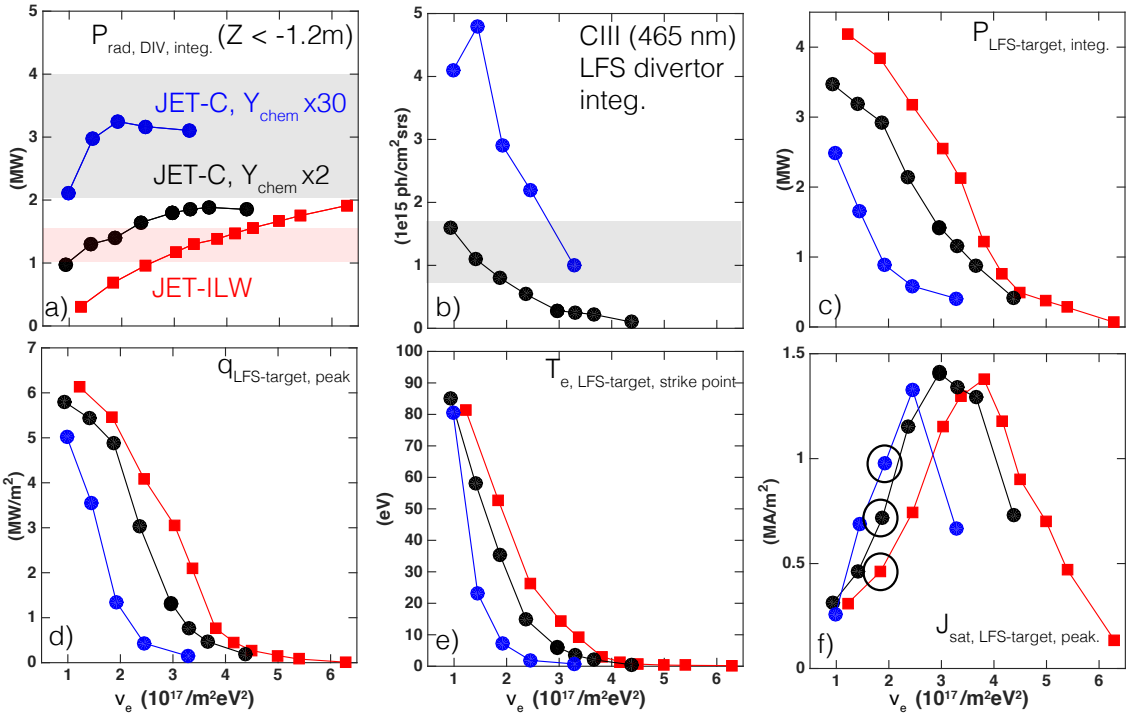
P rad, DIV, integ. (Z < -1.2m)
JET-C, Y chem x30
JET-C, Y chem x2
JET-ILW
a)
(MW)
CIII (465 nm)
LFS divertor
integ.
b)
(1e15 ph/cm2srs)
P LFS-target, integ.
c)
(MW)
q LFS-target, peak
d)
(MW/m2)
T e, LFS-target, strike point
e)
(eV)
J sat, LFS-target, peak.
f)
(MA/m2)
ve (10^17 /m2eV2)
ve (10^17 /m2eV2)
ve (10^17 /m2eV2)

Figure 12.

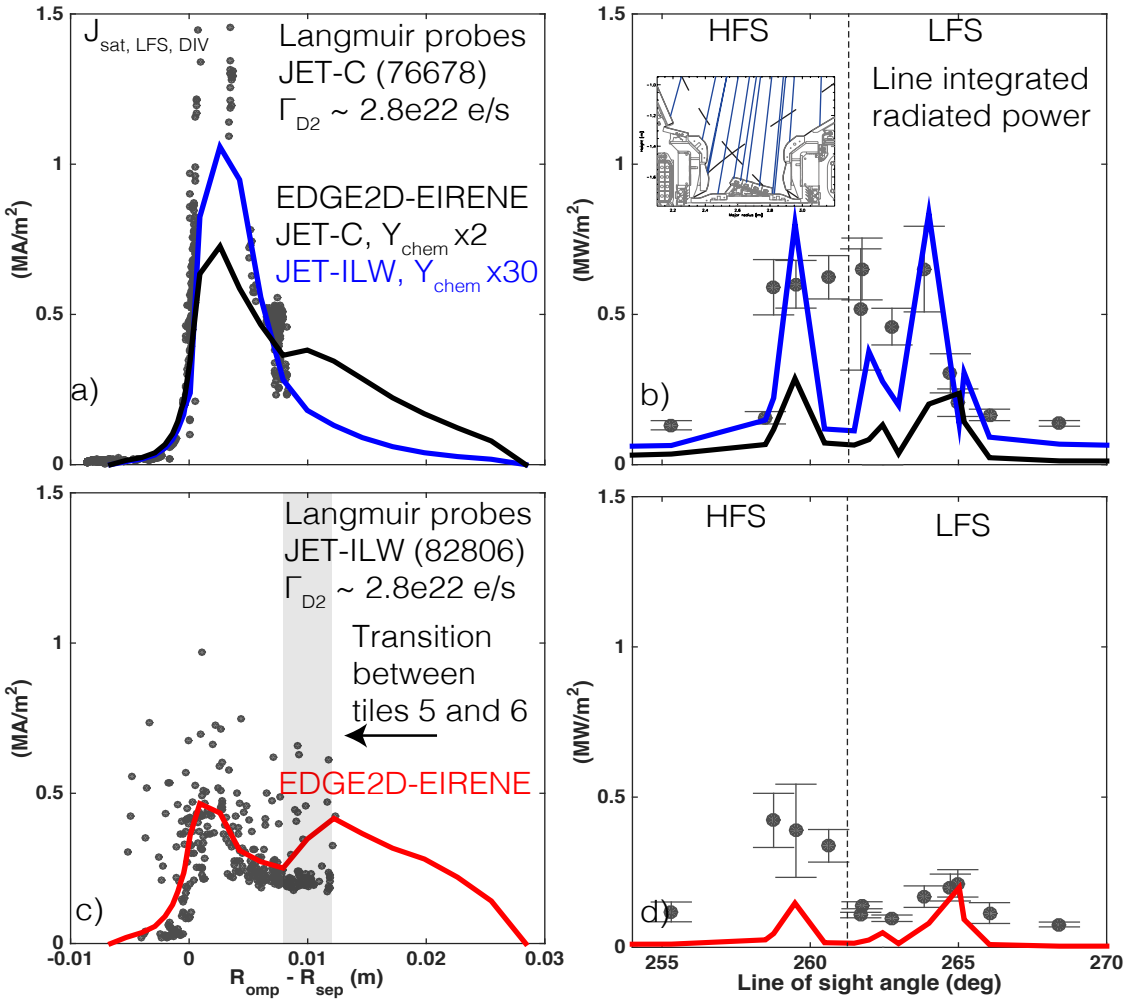
J sat, LFS, DIV
Langmuir probes
JET-C (76678)
Γ D2 ~ 2.8e22 e/s
EDGE2D-EIRENE
JET-C, Y chem x2
JET-ILW, Y chem x30
a)
(MA/m2)
HFS
LFS
Line integrated
radiated power
b)
(MW/m2)
Langmuir probes
JET-ILW (82806)
Γ D2 ~ 2.8e22 e/s
Transition
between
tiles 5 and 6
EDGE2D-EIRENE
c)
R omp - R sep (m)
d)
Line of sight angle (deg)

Figure 13.

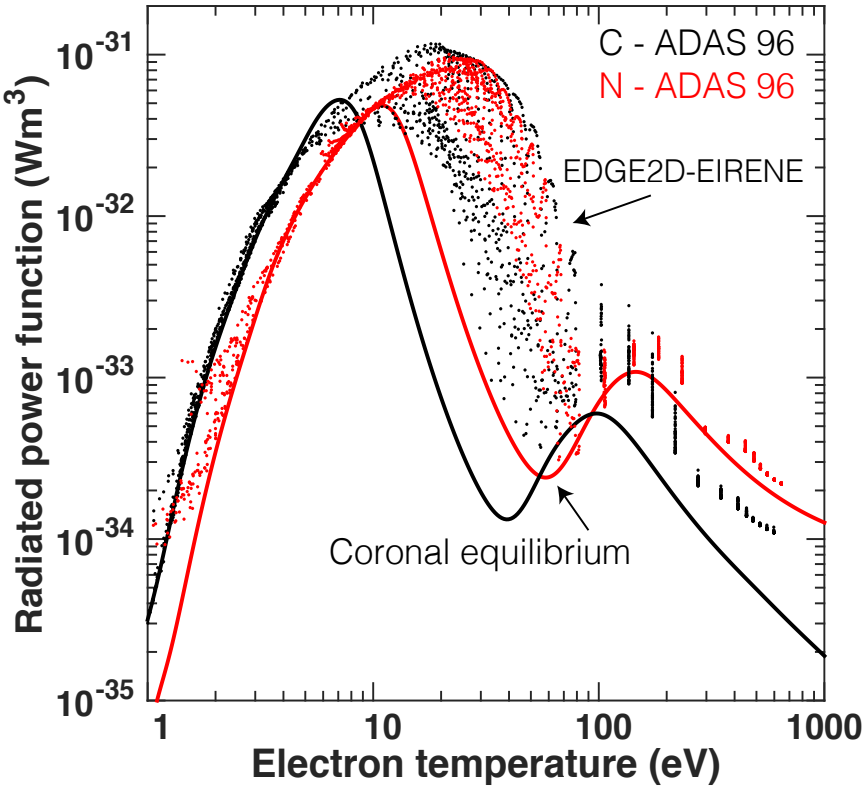
C - ADAS 96
N - ADAS 96
EDGE2D-EIRENE
Coronal equilibrium
Radiated power function (Wm3)
Electron temperature (eV)
10-31
10-32
10-33
10-34
10-35
1
10
100
1000

Figure 14.

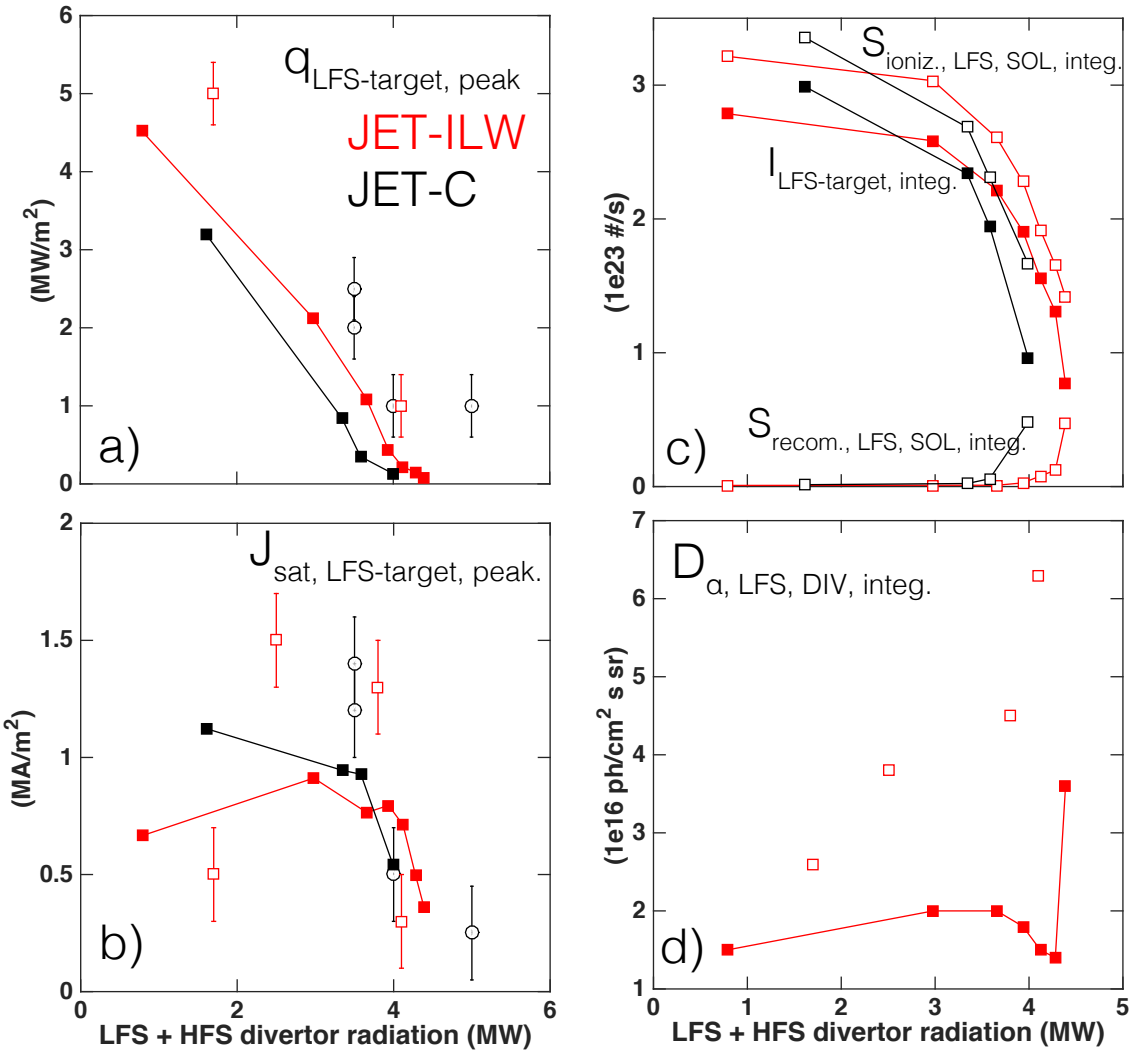
q LFS-target, peak
JET-ILW
JET-C
(MW/m2)
a)
S ioniz., LFS, SOL, integ.
I LFS-target, integ.
S recom., LFS, SOL, integ.
(1e23 #/s)
c)
J sat, LFS-target, peak.
(MA/m2)
b)
D α, LFS, DIV, integ.
(1e16 ph/cm2 s sr)
d)
LFS + HFS divertor radiation (MW)
LFS + HFS divertor radiation (MW)